공학박사 학위논문

Generalized Driving Risk Assessment in Highway Using Risk Field Approach

리스크 필드 접근법을 활용한 고속도로의 일반화된 주행위험 평가기법 개발

2023년 2월

서울대학교 대학원

공과대학 건설환경공학부

주 양 준

Generalized Driving Risk Assessment in Highway Using Risk Field Approach

지도 교수 김 동 규

이 논문을 공학박사 학위논문으로 제출함

2023년 2월

서울대학교 대학원

공과대학 건설환경공학부

주 양 준

주양준의 공학박사 학위논문을 인준함

2023년 2월

위 원 장 _____ 이 청 원 _____ **(인)**

부위원장 _____ 김 동 규 _____ **(인)**

위 원 _____ 고 승 영 _____ **(인)**

위 원 _____ 박 신 형 _____ **(인)**

위 원 _____ 박 준 영 _____ **(인)**

Generalized Driving Risk Assessment in Highway Using Risk Field Approach

Advisor: Dong-Kyu Kim

Submitting a Ph.D. Dissertation of Engineering

February 2023

Graduate School of Engineering

Seoul National University

Civil & Environmental Engineering

Yang-Jun Joo

Confirming the Ph.D. Dissertation written by

Yang-Jun Joo

February 2023

Chair	**Chungwon Lee**	**(Seal)**
Vice Chair	**Dong-Kyu Kim**	**(Seal)**
Examiner	**Seung-Young Kho**	**(Seal)**
Examiner	**Shin Hyoung Park**	**(Seal)**
Examiner	**Juneyoung Park**	**(Seal)**

Abstract

This study provides a generalized method, which visually captures multiple conflicts in various scenarios, for assessing the driving risk encountered by on-road vehicles for driver support and automation systems. To this end, this study employs risk field theory. The risk field approach defines any obstacle to a vehicle as a finite scalar field using the predictive position of the obstacle. This study proposes a modified risk field called the conflict field that captures the driver's subjective risk perception to quantify the level of conflict. The proposed conflict field provides a visually intuitive basis to assess the extent of the conflict and proactively quantifies the risk of the situation in real-time

This study compares the proposed method with existing conflict measures for three driving situations (i.e., car-following, yielding, and lane changing) using highway naturalistic driving data. As a result, the proposed method imposes a higher risk for multiple risky interactions than for a single risky interaction and is generally consistent with post-encroachment time (PET). Lastly, a sensitivity analysis investigates the parameters assumption and the predictive position's bias and variance. The major innovative aspect of this study is to simultaneously assess the various types of multiple conflicts with adjacent vehicles and provide their potential conflict locations. Therefore, the proposed driving risk assessment method can provide robust and stable safety criteria for the

autonomous vehicle system in a generalized way.

Keywords: Risk field, Generalized driving risk assessment, Traffic conflict, Real time risk assessment

Student Number: 2018-27038

Contents

List of Figures

List of Tables

Chapter 1. Introduction

1.1. Background

While there have been substantial improvements in autonomous vehicle (AV) technology in recent years, the safe operation of autonomous vehicles (AVs) remains a concern. Passengers will likely be hesitant to use AVs unless AV technology can demonstrate a high safety level enough to overcome users' psychological barriers and fears (Shariff et al., 2021). These barriers and fears include a possible AV algorithm malfunction in an emergency and an unknown consequence due to the inevitable interactions with pedestrians and motorcycles. In addition, aggressiveness in the driving behavior of human drivers in non-AV vehicles when interacting with AVs can cause potentially risky situations (Lee et al., 2021). These concerns have raised attention to assessing the risk associated with AV operations in a mixed traffic environment, where AV and non-AV are mixed. Unfortunately, ensuring that AV maneuvers are safe in mixed and resultantly complex traffic conditions where there could be countlessly different driving situations is arguably very challenging. It is mainly due to significant differences in adjacent human drivers' reaction time, aggressiveness, and many other unobserved heterogeneities (Arun et al., 2021b; Ba et al., 2016; Mannering and Bhat, 2014; Taeihagh and Lim, 2019).

AVs constantly adjust their driving maneuvers as they recognize surrounding vehicles and other moving objects as obstacles to avoid (Chen et al., 2021; Katrakazas et al., 2015; Machado-León et al., 2016). The technology in an AV continuously updates the risk associated with the possible trajectory of the AV by continuously estimating the trajectories of adjacent obstacles (AVs, non-AV vehicles, pedestrians, street furniture, etc.) (G. Li et al., 2021). Previous studies have tried to quantify the risk associated with these obstacles by using traffic conflict indicators (Arun et al., 2021a). Traffic conflicts occur far more frequently than actual crashes. For that, it is easier to estimate the risk associated with conflicts than to evaluate crash risk in real-time. Typical conflict indicators and their predefined threshold differentiate traffic situations into two possibilities: conflict and non-conflict situations (Arun et al., 2021a; Zheng and Sayed, 2019).

Driving situations vary widely according to numerous factors, including intersection geometry (four-leg intersection, roundabout, etc.), conflict type (angle, rear-end, etc.), and road user types (vehicle, pedestrian, motorcycles, etc.) (Arun et al., 2021b, 2021a; Wang et al., 2021a). Previous studies have noted the importance of the choice of appropriate conflict indicators and their associated thresholds to ensure that the choice made is appropriate for the driving situation and roadway environment (Shi et al., 2018; Wang et al., 2018; Zheng and Sayed, 2019). For example, the time-to-collision (TTC) and modified time-to-collision

(MTTC) are known to be the two most popular conflict indicators for rear-end collision, whereas the post-encroachment time (PET), the lane change risk index (LCRI) are more appropriate measure to estimate the conflicts during the lane changing situation (Chen et al., 2021; Park et al., 2018; Zheng and Sayed, 2019).

The situation-dependent conflict indicators fragment the risk assessment model, using different conflict indicators depending on the specified driving situations. The fragmented model splits a vehicle's moving trajectories (or itineraries) into small pieces called fragments and applies the most suitable conflict indicators that could be different for each fragment (Scholtes et al., 2021). However, switching between conflict indicators according to the possibly widely different driving situations in numerous fragments is hard to provide a continuous risk assessment as the approach cannot guarantee seamless transitions between different driving situations (Kolekar et al., 2020). The conflict indicators and associated thresholds must be matched to continuously changing driving situations for the fragmented model to function correctly. Yet, it is impossible, a priori, to identify all possible driving situations, match the driving situations to the most appropriate conflict indicators, and determine the optimal thresholds for each conflict indicator according to the vast number of different driving situations (Arun et al., 2023, 2022; Mannering and Bhat, 2014).

Although some recent studies try to apply multiple conflict

indicators to estimate the risk for more than one driving situation, further research is still needed to mitigate the challenges associated with applying situation-dependent conflict indicators in risk assessment (Arun et al., 2022; Shi et al., 2018). Especially for AVs, the current fragmented model cannot provide a seamless risk assessment of the AV's anticipated short-term trajectory for motion planning, which designs the AV's anticipated short-term driving behaviors (moving trajectory) over time (G. Li et al., 2021). It is partly because the AV's anticipated short-term trajectories on public roadways can be too many at a level that engineers cannot easily match proper conflict indicators to all possible driving situations (Wang et al., 2019). In addition, the conflict indicators mainly assess the rear-end crash risk for one pair. Therefore, if multiple vehicles interact simultaneously, it is necessary to distinguish which vehicle is primarily in conflict clearly.

In physics, a field (e.g., gravitational, electric, or magnetic field) is represented as the distribution of a physical space. Field theory is an area of study that investigates the rules of motion for moving objects and the objects' interactions within a predefined study field. Some recent studies have proposed using field theory to develop a risk field based assessment for potential traffic crashes (Kolekar et al., 2020; Lee and Kum, 2019; G. Li et al., 2021a; Mullakkal-Babu et al., 2020). The risk field-based assessment assumes that every vehicle and road user generates a series of risk fields on their anticipated short-term trajectories

while traveling on a roadway (Kolekar et al., 2020; Tan et al., 2021). The risk field defines any obstacle to a vehicle as a finite but continuously varying scalar field in each moment that should be avoided (Mullakkal-Babu et al., 2020). According to this risk field based approach, AVs (and indeed any vehicle) can continuously estimate a level of risk and determine their short-term driving maneuvers (e.g., acceleration/deceleration and steering) as appears appropriate according to the estimated level of risk (Kolekar et al., 2020; Lee and Kum, 2019; G. Li et al., 2021; Mullakkal-Babu et al., 2020).

A risk field-based assessment has been applied to evaluate the risk associated with car-following driving behaviors by investigating interactions between two moving objects (e.g., vehicles and pedestrians) and interactions between moving objects and static objects (e.g., road boundary and traffic signals) (Tan et al., 2021). Arun et al. (2023) provide the most recent field theory-based assessment application by estimating possible traffic conflicts between vehicles at signalized intersections. They reported that their risk field-based approach produced more accurate results in predicting crash frequencies as well as crash severities than existing conflict indicators. Arun et al. also stated clearly in the study that this approach can greatly enhance the real-time risk assessment involved with AVs. Our study, therefore, can be regarded as an extension of Arun et al.'s (2023) research in the sense that we also applied the field theory to estimate the risk of AVs under diverse traffic situations (car-

following, lane-changing maneuvers, etc.) and tried to evaluate the safe operation of AVs on future roadways real-time basis(Arun et al., 2023).

1.2. Study goals and objectives

The main goal of this study is to propose a generalized method of assessing the driving risk involved with AVs and non-AVs operation real-time basis. Notice that this approach imitates the human driver's risk perception procedure and proposes a conflict field, which is defined as the overlap in risk fields generated by different vehicles (AVs and non-AVs). The conflict field is designed to capture the perceived risks caused by all possible interactions between adjacent vehicles driving in close proximity. We use field theory to quantify and visualize the holistic risk of various driving situations. The specific objectives of this study are to:

1) Formulate a generalized risk assessment method that can be applied to various driving situations that can include multiple interactions between AVs and non-AVs;
2) Visualize the AVs' perceived risk in a 3-dimensional risk field and provides a quantitative estimate of the total risk for adjacent traffic users (non-AVs);
3) Develop an approximation method for accelerating computation to be used in real-world traffic situations real-time basis

4) Compare the proposed approach with two widely used existing conflict indicators (TTC, MTTC, and PET) under three distinct traffic situations (car-following, yielding, and lane-changing situations).

The rest of this paper is organized as follows. Section 2 provides the case study site (i.e., US-101 highway), data preprocessing procedure, and the analysis scenarios. Chapter 3 briefly introduced a deep-learning prediction model to design the risk field and provide three steps to reproduce our proposed method. First, it introduces a noble concept of the conflict field. Second, it provides a risk field design procedure with the predictive trajectory distribution. Third, it provides an approximation method to integrate the values in the conflict field in real time. Chapter 4 exhibits overall scenarios, compares the proposed method and conflict measures (i.e., TTC and PET) and discusses this study's key findings. At the last part of Chapter 4, this study performs sensitivity analysis on the parameter and the prediction model performance. Finally, Chapter 5 concludes the study and discusses future work.

Chapter 2. Literature Review

2.1. Surrogate safety of measures (SSM)

2.4.1. Strength of SSM

Since the late 1960s, Surrogate safety measures (SSM) have been used to analyze road safety. Due to the benefits of using SSM, it serves as the basis for proactive countermeasure preparation. SSM is an indicator that evaluates driving safety through proxy indicators that can express safety instead of analyzing past crash history to evaluate the driving safety of vehicles. SSM provides insight into crash analysis by identifying the cause of the collision, accompanied by the risk profile, compared to safety assessments using only the data of observed accidents.

Traditionally, road safety analysis analyzes crash data to predict collision probability. However, this approach has numerous drawbacks:

1) Crash data analysis is reactive. It is practically difficult to attain the aim of zero traffic fatalities and serious injury collisions since safety evaluation depends on collisions occurring to evaluate the level of safety.

2) Due to the crash's rarity, at least five to ten years of crash data are typically required for the number of crash to be statistically significant. During this time, intersection configurations and road user patterns may substantially change.

3) Crashes and injuries are underreported in many localities, rendering crashes data incomplete and occasionally unreliable.

Due to these factors, numerous road safety studies have turned to SSM. The SSM techniques aim to shorten the data collection cycle by identifying specific surrogate indicators highly correlated to the risk of collisions, which occur much more frequently than collisions. Unlike crash studies, which require many years of data, surrogate safety studies require only 30 to 60 hours of trajectories from nearly any camera or LiDAR, making it a time- and cost-efficient method(Arun et al., 2022; Essa and Sayed, 2019; Fu and Sayed, 2022).

The hierarchy of road user interactions ranges from undisturbed passengers (no interaction or proximity whatsoever) to fatal crashes. SSMs enable the indirect observation of crashes by examining interactions that are considered crash precursors. By examining interactions in serious, modest conflicts, and undisturbed interaction, one may collect data that allows us to estimate the likelihood of severe crashes. In previous studies, SSM has been estimated to have a close relationship with crashes (Arun et al., 2021b, 2021a). In particular, traffic conflict techniques have commonly been used to define traffic conflicts in events where SSM crosses predefined thresholds.

2.4.2. Types of SSM

Since SSMs are aimed at quantitatively describing dangerous situations, conflicts can be evaluated from various perspectives, such as temporal, spatial, and kinematic proximity. Among the SSMs, temporal proximity measures were the most widely applied. Time-to-collision (TTC) and Post-encroachment time (PET) were the most widely used temporal proximity measure. **Equation 1** and **2** shows TTC and PET, respectively.

$$TTC_i = \frac{\Delta d(t)}{\Delta \mathrm{v(t)}} \forall \Delta \mathrm{v(t)} > 0 \qquad (1)$$

Where,

$\Delta \mathrm{d(t)}$: relative distance

$\Delta \mathrm{v(t)}$: relative speed

$$\mathrm{PET} = T_b - T_a \qquad (2)$$

Where,

T_b : Time of ego vehicle′s conflict point

T_a : Time of preceding vehicle′s conflict point

Temporal crash proximity measures capture the intensity of conflicts in terms of time immediately before a crash, regardless of the application context(Arun et al., 2021a). TTC and PET express the temporal proximity to crash as a time. TTC represents the time it takes to reach the collision point when the two observed road users maintain their current speed and direction. On the other hand, PET corresponds to the time difference when one road user enters this point after exiting the expected collision point. Both TTC and PET can be used for all interactions, but most previous studies have used TTC to indicate the risk of rear-end crashes. When the predicted trajectories of road users intersect, PET has been used most frequently. As a variant on TTC, Modified-TTC (MTTC), which assumes that the current acceleration is maintained up to the point of collision, is proposed to complement the constant velocity assumption of TTC(Essa and Sayed, 2019). **Equation 3** shows MTTC.

$$MTTC(t) = \frac{-\Delta v(t) \pm \sqrt{\Delta v(t)^2 + 2d(t) \cdot \Delta a(t)}}{\Delta a(t)} \forall \frac{1}{2} \Delta a(t) t^2 + \Delta v t > d(t) \quad (3)$$

Where,

$\Delta v(t)$: relative speed

$\Delta a(t)$: relative acceleration

$\Delta d(t)$: relative distance

Although MTTC was reported to have a higher correlation with accidents than TTC in a study by Essa et al., 2019, additional verification is needed for other study sites (Essa and Sayed, 2019). Other indicators modifying TTC include time-integrated time-to-collision (TIT), which indicates the degree to which TTC falls below a specific threshold (Rahman et al., 2019). However, few studies used it to capture temporal proximity. **Equation 4** shows TIT.

$$\int_0^T [TTC^* - TTC(t)]dt,\ \forall 0 \leq TTC(t) \leq TTC^* \quad (4)$$

Where,

$TTC(t)$: TTC at time t

TTC^*: Traffic conflict threshold

In addition, SSMs such as spatial proximity, kinematic indicators, and their mixing and combinations are also applied to the crash analysis depending on the application context (e.g., road geometry, study site). However, although various SSMs have been used, a verification study on the appropriateness of SSMs is needed for all different types of traffic conditions. Few studies have been undertaken on the relationship between SSM and incidence, and the context of SSM application has been largely neglected. SSM development applicable to various traffic

situations, including vulnerable road users such as pedestrians and motorcycles, is a viable solution for safety research by replacing existing SSMs requiring verification for numerous traffic scenarios.

Spatial proximity measures capture proximity to crash in terms of space. For example, Stopping sight distance (SSD) measures the required distance to stop a vehicle when decelerating after the driver's reaction time (typically 1.5 ~ 2.5 sec). **Equation 5** shows SSD.

$$SSD(t) = \frac{v(t)^2}{254 \times (f+g)} + reaction\ time\ \times v(t)\ \times 0.278 \qquad (5)$$

Where,

$v(t)$: speed of vehicle [km/h]

f: friction coefficient

g: grade with decimal

The spatial proximity measures have been used to measure conflicts with relatively low frequency. The main reason is that the spatial proximity measurement method is suitable only for measuring long-distance conflicts. For example, it is unsuitable for urban traffic situations, such as intersections requiring relatively short distances, because it is valid only for conflicts encountered at high speeds over long distances, such as highways (Park et al., 2018).

SSMs can be mixed to represent to illustrate the complex conflict process. For example, the aggregated crash propensity metric (ACPM) evaluates the driving safety of the current situation by comprehensively utilizing four indicators: TTC, reaction time, required deceleration rate, and maximum available deceleration. It assumes various factors, such as occupancy of nearby lanes, and the possibility of changing direction and speed, jointly affect the current driving situation's risk(Wang and Stamatiadis, 2014). However, since the researcher's subjectivity plays a significant role in creating the formula for mixed indicators, further research is still needed to quantify the strength of the generally used avoidance maneuver. Accordingly, there is a limit to using verified indicators in measuring crash risk.

The simultaneous use of various SSMs can be expressed as a combination of indicators. The difference from mixed indicators that use multiple indicators simultaneously is that they are not expressed as a single value. For example, an event in which a TTC or deceleration rate falls below a specific threshold can be defined as a conflict. The method of measuring conflict through various indicators describes only a fraction of the individual SSMs conflict, so all kinds of conflicts can be measured by using multiple indicators comprehensively. Of the 386 studies conducted between 2010 and 2019, 27% used one or more SSMs. Of the studies using one or more SSMs, 43% used TTC and PET (Arun et al., 2021b). In the case of the predictive performance of an accident, it was

reported that the predictive performance was better when predicting using two indicators than when TTC and PET were used alone (Arun et al., 2022; Essa and Sayed, 2019).

Unlike the presented SSM, the crash severity SSMs aim to measure the crash's severity when it occurs. It is generally accepted to assume that the expected crash severity is proportional to the amount of impact generated at the time of the collision. The motion caused by the crash is inelastic; thereby, the two vehicles move simultaneously after the crash. The popular crash severity SSM is the deceleration rate to avoid collision (DRAC) given by **Equation 6** and **7**

$$DRAC = \frac{(v_2 - v_1)^2}{2d_{12}} \ \forall \ \mathrm{v}_2 - \mathrm{v}_1 > 0 \qquad (6)$$

$$Delta - V = \frac{m2}{m_1 + m_2}\sqrt{v_1^2 + v_2^2 - 2v_1 v_2 cos\theta_{12}} \qquad (7)$$

Where,

v_1, v_2 : speed of vehicle 1 and 2

d_{12} :distance between vehicle 1 and 2

m_1, m_2 : mass of vehicle 1 and 2

θ_{12} : steering angle between vehicle 1 and 2

The Severe Crash Metric (SCM) is calculated using the exponential of the Delta-V, and the aggregated severe crash metric (ASCM) is the average of the probabilities of crashes given severity type.

ASCM are estimated conditionally on time-to-collision (TTC), maximum available deceleration rate (MADR), and driver's reaction time (RT). **Equation 8** and **9** shows Severe Crash Metric (SCM) and ASCM.

If $\mathrm{RT} < \mathrm{TTC}$; or
If $\mathrm{RT} > \mathrm{TTC}$ and $\mathrm{DRAC} > \mathrm{MADR}$; then

$$\text{Severe Crash Metric (SCM)} = \left(\frac{\Delta v_1}{\alpha}\right)^{\beta} + \left(\frac{\Delta v_2}{\alpha}\right)^{\beta} - \left(\frac{\Delta v_1}{\alpha}\right)^{\beta}\left(\frac{\Delta v_2}{\alpha}\right)^{\beta} \quad (8)$$

$$\mathrm{ASCM} = \sum_{i,j} \mathrm{SCM}, \quad (9)$$

Where,

i, j: index of conflicting pairs of vehicles.

α: Constant parameter

Laureshyn et al., proposed Extended Delta-V considering deceleration after crash (Laureshyn et al., 2017). **Equation 10** and **11** shows modified v for extended Delta-V.

$$v_1 = \begin{cases} v_{01} - a_1 t, if(v_{o1} - a_1 t) \geq 0 \\ 0,\ otherwise \end{cases} \quad (10)$$

$$v_2 = \begin{cases} v_{02} - a_2 t, if(v_{o2} - a_2 t) \geq 0 \\ 0,\ otherwise \end{cases} \quad (11)$$

Where,

v_{01}, v_{02}: the initial speeds (m/s) of the ego and conflicting vehicle at the start of the conflict,

t : the duration of conflict (sec).

a_1, a_2 : deceleration rate during conflict

Then Delta-V is calculated as the formula given above. Ma et al proposed another severity SSM considering its crash angle(θ) with the delta kinetic energe (ΔKE), as show in **Equation 12** (Ma et al., 2018).

$$\Delta KE = \frac{1}{4}(v_1^2 + v_2^2) - \frac{1}{2}v_1 v_2 cos\theta_{12} \quad (12)$$

Where,

v_1, v_2: speed of vehicle 1 and 2

θ_{12}: steering angle between vehicle 1 and 2

Comprehensive safety often consider both the severity of the accident and the frequency of the accident. In order to express the indicators representing this at once, it is common to define and use the indicators representing accident severity and accident frequency in the form of multiplication. As an example, the event failure index captures overall driving risk, proposed by Park et al. (2018). **Equation 13** shows the event failure index.

$$\text{Event failure index} = \text{REL} \times \text{RSL} \quad (13)$$

Where,

Risk exposure level (REL): the ratio of exposure to a dangerous situation

Risk severity level (RSL): the expected accident severity of the situation.

The SSM sets a specific threshold and defines a conflict and non-conflict state. Therefore, depending on threshold's choice, the pattern of conflict and the relationship between accidents appear differently—failure to properly select the threshold results in the wrong safety countermeasures. A study by Essa et al. (2015) showed that the linear relationship was significantly changed by the threshold of SSM in the conflict measured through simulation (Essa and Sayed, 2015). Therefore, the choice of SSM threshold should consider the context of the conflict, as the choice of SSM.

2.2. Field theory-based risk assessment

2.2.1. Potential field indicator

Field theory originated from physics, which defines the distribution of physical forces between particles as fields and explains the relationship through the physical field. When simulating the movements of road users, human safety motivations and safety-relevant behaviors must be taken into account in addition to the normal dynamics of road users. As a result, previous research has aimed to simulate the inherent importance of safety in driving decisions, particularly in robotic route guidance and path planning.

The risk field, which had no clearly defined bounds, indicated the range of potential routes that a vehicle may take at any one time, assuming that no other objects were in the way. The risk field postulate the concept of "valence" or an object's appeal, and stated that the safe travel area has a positive valence that directs the vehicle (ref). As a result, acceleration was the action taken to reach the desired velocity, and steering was the drivers' series of responses to objects of negative valence that helped them keep the vehicle heading towards the middle of the field of safe travel. The ego vehicle took evasive action within a minimal stopping zone if the field of safe travel of one vehicle.

By introducing an artificial potential field function to direct robot motions in a physical environment, previous studies operationalized this

theory in the field of robotics. The artificial potential formulated a repulsive component that governs collision avoidance and an attracting component that directs the robot's movement in the desired direction. The repulsive force was defined as the negative gradient of the potential field containing the obstacles and the movement destination located at the global energy minimum. These two components together represent the overall potential at any one time, which acts as a virtual force on the robot and vehicle.

The field theory-based risk assessment approach assumes that just as two particles have the force to repel each other, the vehicle also has the force to repel each other. **Figure 1** shows the relationship between particles and the vehicle safety assessment based on field theory.

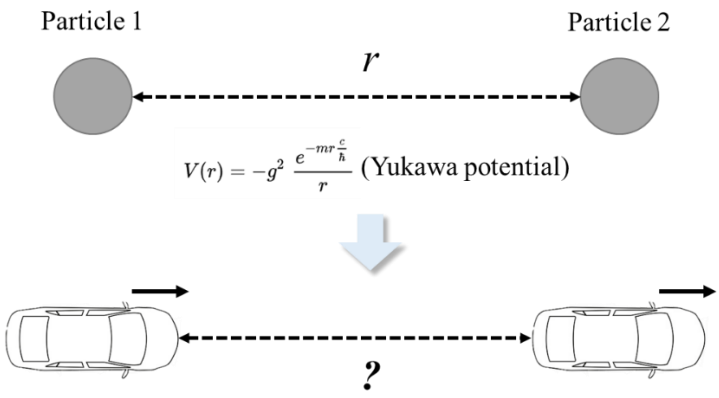

Figure 1. Conceptual diagram of safety evaluation based on field theory

The force acting between two typical particles is expressed as Yukawa potential. Yukawa potential is shown in **Equation 14**.

$$V(r) = -g^2 \frac{e^{-mr\frac{c}{\hbar}}}{r} \tag{14}$$

Where,

$V(r)$: magnitude of the potential generated around the particle,

m: the particle's mass.

r: the distance from the particle.

Yukawa potential's potential decreases as the distance r from the particle increases, and so does the force's magnitude. It is a risk field-based safety assessment technique that defines the forces between vehicles by applying the field theory concept found in physics.

The formulation of intensity generated by vehicles is an actively studied area. Since the literature has employed a variety of functional forms, including Gaussian and Yukawa potential, choosing a functional form for the risk potential is a crucial decision. The particles of Yukawa potential do not consider the shape of the field generated by the particles' motion; thus, it is not easy to apply them in the same manner to the vehicle. In addition, unlike particles, the vehicle has different volumes and masses, and the driving characteristics vary depending on the driver,

so there is a lack of generalized indicators. This chapter reviews the potential functions expressed in previous studies for applying the risk field (or safety potential field), and the implications are derived accordingly.

A field with the potential to push out surrounding objects created by the vehicle (by threatening them) is called a risk field. Li et al. (2020) defined the risk field's intensity with the vehicle's dynamic state, including equivalent mass, speed, acceleration, and steering angle. The mathematical expression of equivalent mass is shown as **Equation 15**.

$$M_i = m_i \cdot (1.566 \cdot 10^{-14} \cdot v^{6.687} + 0.3345) \tag{15}$$

Where,

M_i : the equivalent mass of object vehicle i

m_i : its actual vehicle mass.

The equivalent mass increases as velocity increases; therefore, the safety risk of the object vehicle at high speed is significantly greater than that of the vehicle at low speed.

During the driving process, an object vehicle's sphere of influence is limited; it will only affect a small number of neighboring vehicles. With increasing distance, the influence will diminish significantly. The interaction between two cars is analogous to the

interaction between two particles, as represented by the Yukawa potential. Li et al. (2020) constructed a vehicle potential field function in response to this and the preceding influence factor study, as shown in **Equation 16**.

$$E_v = M_i \cdot \lambda \cdot \frac{e^{-\beta_1 cos\theta}}{\left(\sqrt{[\left(x - x_0 \frac{\tau}{e^{av}}\right]^2 + [(y - y_0)\tau]^2}\right)^{\zeta}} \cdot \frac{k\prime}{|k'|} \tag{16}$$

where,

λ, β_1 : determined coefficients,

θ: the angle formed by any point around the object vehicle

M_i: Equivalent mass center of the object vehicle

a: the acceleration of the object vehicle's current motion state

k': pseudo-distance

The pseudo-distance represents the generalized distance considering vehicle's moving direction and the corresponding risk perceiving. The pseudo-distance is shown by **Equation 17**.

$$k' = \sqrt{[\left(x - x_0 \frac{\tau}{e^{av}}\right]^2 + [(y - y_0)\tau]^2} \tag{17}$$

Where,

ϕ : the clockwise vehicle steering angle

τ: Critical threshold of the safe distance

a: Constant parameter

Equation 10 assumes that a vehicle should maintain a safe distance behind an object vehicle in its lane, although it is permitted to be close to a side obstacle or the road's boundary. They also assumed that driving risk should be similar when the vehicle is 30 m behind the ego vehicle and 2.0 m at the ego vehicle's side.

In **Equation 9**, the equivalent mass corresponds to a charge in the Yukawa potential and decreases exponentially with the distance away from the vehicle's location (x_0, y_0). There is no unit for the force transmitted from the potential to the surrounding vehicle; accordingly, only relative comparison is possible. The magnitude of the force from the potential generated by the risk field is defined by **Equation 18.**

$$F_v^{AB} = -m_B \cdot e^{\beta_2 \cdot v_B \cdot cos\phi} \cdot |E_v^A| \tag{18}$$

Where

F_v^{AB} : to the force of vehicle A from vehicle B,

m_B: the mass of vehicle B

v_B: the speed of vehicle B

ϕ is the steering angle of vehicle B

E_v^A : the size of the risk field generated from vehicle A.

If the magnitude of the force is integrated with the distance, the safety potential field energy (SPFE) can finally be obtained with **Equation 19**.

$$SPFE = -\int_{\infty}^{r_{AB}} F^{AB} dr = -m_B e^{\beta_2 \cdot v_b \cdot cos\phi} \cdot \int_{\infty}^{r_{AB}} |E_v^A| dr \qquad (19)$$

By linearly adding SPFE to multiple vehicles and road geometry as follows, the Potential Field Indicator (PFI) that quantifies the risk felt by the driver can be calculated. PFI is weighted sum of SPFE, as shown in **Equation 20**.

$$PFI^j = \mathrm{w}_L \cdot \mathrm{SPFE}_L^j + \mathrm{w}_B \cdot \mathrm{SPFE}_B^j + \mathrm{w}_V \cdot \mathrm{SPFE}_V^j \qquad (20)$$

Where,

w_L , w_B , w_V : weight of the SPFE of lane, boundary and vehicle, respectively

SPFE of lane and boundary was formulated the samely as **Equation 11**, based on the pseudo-distance *k'* from lane marker and road boundary. Li et al.(2020) did not provide calibrated parameters for constructing SPFE. The

safety potential field parameters of vehicles with varying degrees of autonomy should vary. For model calibration, a substantial amount of real trajectory data of vehicles at each level is still necessary.

2.2.2. Risk force

Arun et al. (2023) proposed risk force quantifying the driver's perceived risk using Coulomb's law, similar to Li et al. (2020) quantified the risk based on Yukawa potential. Coulomb's law is shown in **Equation 21**.

$$E = \frac{1}{4\pi\epsilon}\frac{q_1}{r^2}\hat{r} \tag{21}$$

Where,

E: Potential energy

ϵ: Permittivity of medium

q_1: charge of particle 1

$r, \hat{r}$: the size of vector r and unit vector or r, respectively

Coulomb's law describes that a elctro charged particle generates electromagnetic fields equidistantly according to the amount of charge, the permittivity constant (ϵ), and the distance between particles (r). Risk force risk severity with the Delta-V and vehicle's mass along with speed and steering angle. **Equation 22** shows risk force defined by Arun et al.,

(2023) (Arun et al., 2023)

$$F_{ult,21} = \left|F_{sev,21} \cdot F_{coll,21}\right| \propto (m\Delta v)\frac{v_{r,12}\cos(\theta_{12}-K\alpha_1)}{\epsilon_R} \cdot \frac{Q_1 Q_2}{d_{12}+\Delta d} \quad (22)$$

Where,

$F_{sev,21}$: the risk force of severity.

$F_{coll,21}$: the risk force of collision between vehicle 1, 2,

$F_{ult,21}$: The ultimate risk force

F_{ult} allows for the modeling of the entire traffic interaction and provides estimates of the likelihood of a crash and the severity of the crash. The risk potential (Q_1) of the driver-vehicle combination consider response time and maximum available deceleration rate. **Equation 23** formulate risk potential.

$$Q_1 = (e^{\xi\frac{\beta_{r1}T_{r,1}}{\beta_{v1}b_{max,1}}}) \quad (23)$$

Where,

$T_{r,1}$: the response time of driver 1

$b_{max,1}$: the maximum available deceleration rate.

ξ, β_{r1},β_{v1} : the constant vehicle characteristic constant.

The risk potential is higher for road users with longer response time, while higher $b_{max,1}$ lowe the risk potential. Therefore, the risk potential variable incorporates vehicle-related heterogeneity.

The risk field parameters was fitted based on the crash data on the study site. Arun et al.(2023) estimated proposed parameterse by solving for the roots of for each crash cases with **Equation 24**. A simulated obtimization technique can be applied to fit parameters but was not addressed further in this paper.

$$Minimize\ \sum\left(1 - F_{coll,21}\right)^2 \tag{24}$$

The optimal parameter values were those that produced the predictive power to the crash estimation. However, in Arun et al.(2023)'s study, the parameter was hard to converge using crash history; its coefficient of variance was larger than 10. Therefore, measuring parameters through driving simulators or drivers' biometric data, which can obtain more data, may compensate for these limitations.

As a result of reviewing previous studies, the size of the risk field of the vehicle is determined by the following factors.

1) Vehicle speed: The severity of the crash increases in proportion to the vehicle speed, and the size and shape of the risk field are determined by the speed and direction of the surrounding vehicle.

2) Distance: The closer the distance between the two vehicles, the larger the size of the risk field. Pseudo distance is also used in consideration of the direction of progress.

3) Vehicle mass: The larger the vehicle mass, the greater the impact and the higher the crash severity

4) Types of conflict pair: The size of the risk field varies depending on the type of stationary object (e.g., lane, road boundary) and the moving object (e.g., vehicle, pedestrian, motorcycle).

Chapter 3. Method

3.1. Risk field concept

The risk field forces a vehicle of interest called ego vehicle to follow specific rules to evade collision with the risk field. Each driving situation is assumed to produce a scalar value (i.e., risk) with every point in a two-dimensional physical space called a risk field (Tan et al., 2021). **Equation 25** represents the risk field mapping a scalar value corresponding to all elements X (i.e., x, y coordinates of moving objects) in domain A.

$$\boldsymbol{F} : A \subset \boldsymbol{R}^2 \rightarrow \boldsymbol{R} \tag{25}$$

Figure 2(a) shows a series of possible risk fields illustrated in four different oval-shaped 3D distributions for the vehicle moving on the left-side traveling lane (black vehicle). The area size of a risk field is smaller, with a high peak in the near future position of the vehicle in its anticipated trajectory. On the other hand, the area size of a risk field becomes larger with a flatter peak in relatively farther position of the vehicle in its anticipated trajectory. The small area with a high peak in distribution represents the high probability of a vehicle's anticipated

position in a future trajectory compared to the large area with a flatter peak or vice versa. As a result, we can say that the volumes (i.e., probability) of the 3D distribution of a moving vehicle's four risk fields in this figure are the same, although the distribution height in each risk field decays along with the vehicle's predicted trajectory horizon.

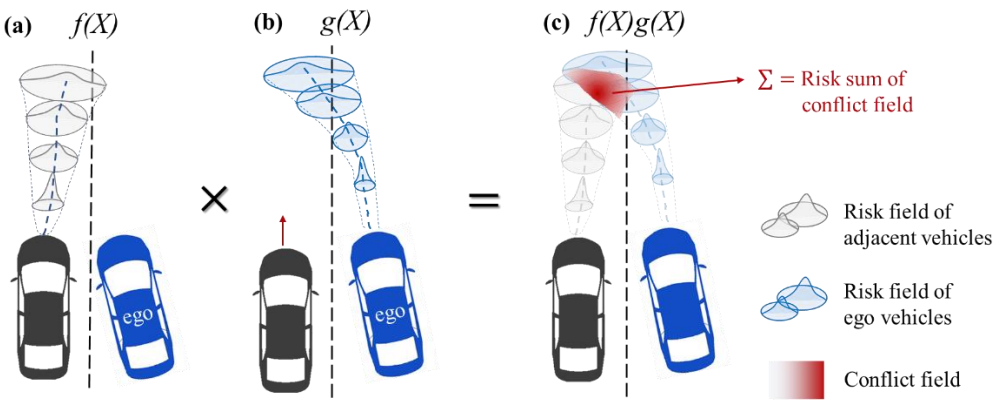

Figure 2. The schematic of the risk fields and their components: (a) risk field of other vehicles, (b) risk field of ego vehicle, and (c) conflict field

In the figure, the ego vehicle's (blue vehicle) estimated risk field will be produced as the same as the other (black) vehicle. Intuitively, the conflict level would be proportional to the extent of overlap between two risk fields in this particular illustration with two moving vehicles (Kolekar et al., 2020). This study formulated a field that represents the extent of conflict as a product of the risk field of other vehicles f(X) (**Figure 2 (a)**) and the ego vehicle's risk field g(X) (**Figure 2 (b)**). We defined this overlapped risk field between moving objects as the "conflict field" as shown in **Figure 2 (c)**.

Figure 2(c) implies that the estimated conflict field will have a zero value if the two risk fields created by the two vehicles do not overlap each other at all, but the value will get greater if the overlapped risk fields from the two vehicles are getting larger and larger. As a result, the risk sum of the conflict field (RSCF), which represents the magnitude of the risk created by the two vehicles, can be obtained depending on the volume of 3D distribution of the two conflict fields. The RSCF can therefore be treated as a safety measure to estimate the perceived risk of ego vehicle each moment. **Equation 26** displays the mathematical formulation of the risk sum of the conflict field, which requires double integration for the two-dimensional risk field at a time t. In the RESULT section, we will demonstrate the implications of RSCF values under three different driving scenarios.

$$RSCF_t = \iint_{g_t(x,y)} f_t(x,y) g_t(x,y) dxdy \tag{26}$$

Where,

$RSCF_t$: Risk sum of the conflict field at time t.

$f_t(x,y)$: the risk field of other adjacent vehicles at time t.

$g_t(x,y)$: the ego vehicle's risk field at time t.

Although this study deals with conflicts with only moving vehicles, field theory can easily be extended to estimate the conflict field

created by various types of obstacles. It includes moving obstacles (e.g., interactions between vehicles and pedestrians) or different types of static obstacles (e.g., interactions between vehicles and road centerlines or traffic control devices such as traffic signals) (Tan et al., 2021).

3.2. Risk field design

Driver perceived a sense of risk objects in their predicted trajectory. The predicted trajectory given historical trajectory is the primary concern in the autonomous vehicle accordingly. Proposed risk field put highly intensity where its predictied probability is high. Trajectory is a continuous history of the vehicle position, but this study employed 0.1 sec of interval for simplication. 0.1 sec is widely used temporal interval in most trajectory studies.

We assumed that trajectory is a 2-dimentional history of the object, ignoring its heigh as it's relationship between risk perceivence was not previously defined. Therefore, integral of predicted distribution of x, y coordinate given historical trajectory $\mathrm{P}(x_t, y_t|X)$ is 1.0, as shown in **Equation 27.**

$$\iint \mathrm{P}(x_t, y_t|X)\, dxdy = 1 \qquad (27)$$

Where,

$\mathrm{P}(x_t, y_t|X)$: probability density of given X at time t.

x_t, y_t : x, y coordinate after t sec.

X : historical records of x, y coordinate

This study made the two basic premises in designing the risk field of moving obstacles: (a) ego vehicle recognizes the object in the space to be occupied by other obstacles as a potentially risky space; (b) drivers tend to discount risks in the future. Therefore, an obstacle's predicted distribution of a more distant future poses less risk to the driver, and the risk field needs to discount the future risk. Lee and Kum (2019) introduced the concept of the advanced time-to-occupancy (ATTO) function to discount future risk. **Figure 3** shows how the ATTO function determines the risk field's strength by weighting the predicted distribution. We assumed that the ATTO exponentially reduced the risk of future occupied space.

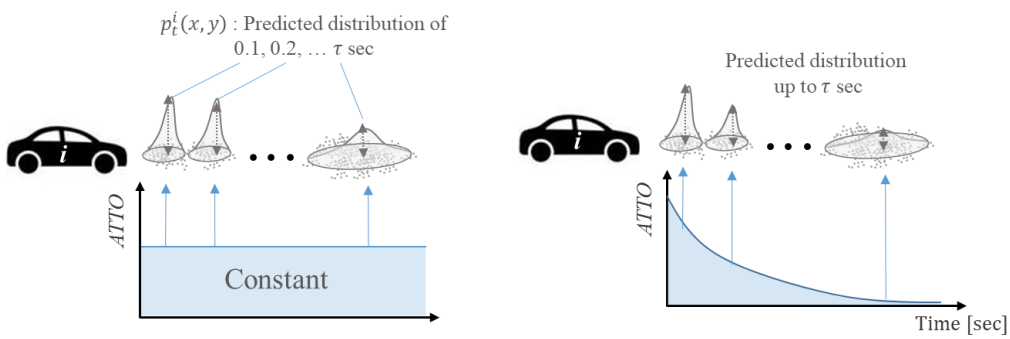

Figure 3. Risk field design with predicted distribution and advanced time-to-occupancy (ATTO)

Equation 28 shows that the proposed ATTO function is to be halved every certain specific period $t_{1/2}$.

$$ATTO(t) = \left(\frac{1}{2}\right)^{\frac{t}{t_{1/2}}}, \tag{28}$$

Where,

$t_{1/2}$: the half-life of the risk field

The half-life was based on the exponential decrease of risk field intensity over distance in Yukawa potential, reflecting an exponential decrease in the degree of feeling danger over time. The half-life represents the driver's insensitivity to danger. The longer the half-life, the more driver feel the risk of the future.

This study introduced an artificial occupancy (AO) that drivers thought occupied in deciding their maneuvers. **Figure 4** shows the artificial occupancy of an object i (AO_i), consisting of three components: bounding box, safety margin, and standstill distance.

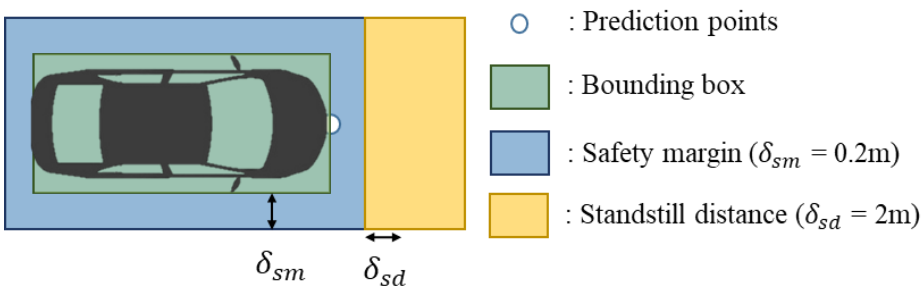

Figure 4. Component of artificial occupancy

First, the safety margin is a buffer for the bounding box, which is the vehicle's occupied space. Drivers erroneously recognize the size of their vehicle and prefer a buffer in their maneuvers, perceiving their vehicle as occupied more than the bounding box. The safety margin would then reduce the effect of measurement errors in onboard sensors and capture conflicts that may occur on the side or in the back of a vehicle. Therefore, increasing the safety margin can lead to a more conservative risk assessment result. We also introduced standstill distance in front of a vehicle to the artificial occupancy like other car-following models (e.g., the intelligent driver model).

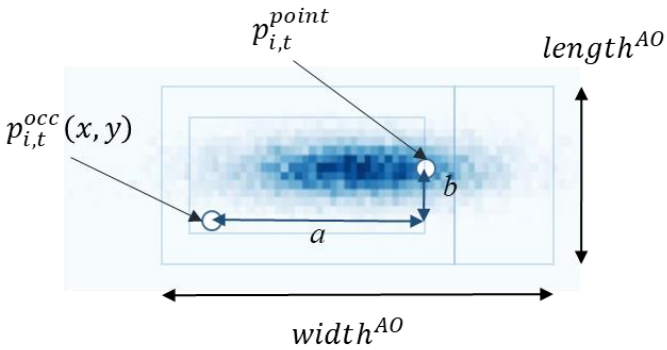

Figure 5. Schematic of notations in occupancy distribution

Figure 5 shows transforming prediction points, a prediction model's output, into a 2-dimensional artificial occupancy for estimating the predictive occupancy distribution $p^{Occ}(x,y)$. **Equations 29** and **30** define the predictive occupancy of object i for time t $p_{i,t}^{Occ}(x,y)$ with the predictive probability of the points $p_{i,t}^{point}$.

$$p_{i,t}^{Occ}(x,y) = p_{i,t}^{point}(x+a, y+b) \tag{29}$$

$$a, b \sim Uniform(width^{AO}, length^{AO}) \tag{30}$$

Where,

$p_{i,t}^{point}$: predicted probability of x, y coordinate of object *i* at time *t*

$p_{i,t}^{Occ}(x,y)$: predicted occupancy distribution of x, y coordinate of object *i* at time *t*

$p_t^i(x,y)$ is point distribution provided by the prediction model.

All areas occupied by the object are assumed to have the same value as the prediction points. **Figure 6** shows the schematic of the transformation procedure.

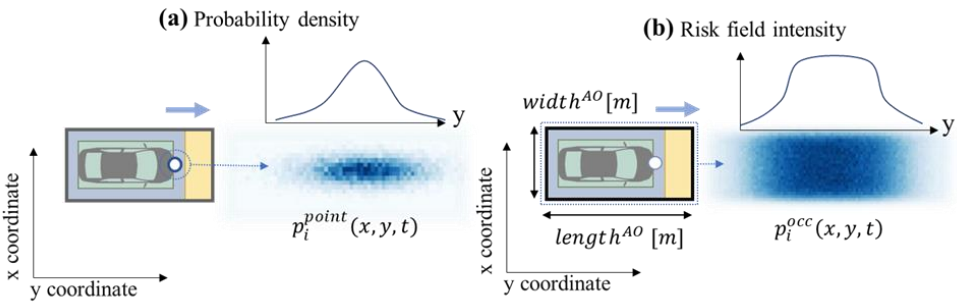

Figure 6. Schematic of point probavility density (a) and risk field intnsity (b)

The driving risks of vehicles are different under different velocities. Previous studies utilized the concept of equivalent mass to take this property in the risk field (Li et al., 2022; Wang et al., 2016). The mass of a vehicle in motion can be defined as a kind of equivalent mass that is proportional to the vehicle's current velocity and reflects the degree of driving risk at a given speed. The mathematical expression of equivalent mass suggested by (Wang et al., 2016) is used. **Equation 31** shows the equivalent mass of the vehicle.

$$f_i(x,y) \propto M_i = m_i(1.566 \cdot 10^{-14} v_i^{6.687} + 0.3345) \tag{31}$$

Where,

m_i: mass of vehicle i

v_i: speed (km/h) of vehicle i

We assumed that the mass of the vehicle (m) is proportional to its bounding box's width and length, regardless of the type of vehicle. Finally, the risk field $f_t(x,y)$ is formulated as the product of the $ATTO(t)$ and $p_{i,t}^{Occ}(x,y)$ integrating over time t until prediction horizon τ, as **Equation 32** and **33**. The risk field's value has no unit; thus, only a relative comparison is possible. Figure 6 (b) shows exemplary risk and conflict fields.

$$f_i(x,y) = M_i \cdot \frac{1}{\varphi_i} \int_{t=1}^{\tau} p_i^{Occ}(x,y,t) \cdot ATTO(t)dt$$

$$= \frac{m_i(1.566 \cdot 10^{-14} v^{6.687} + 0.3345)}{\varphi_i} \int_{t=1}^{\tau} p_i^{Occ}(x,y,t) \cdot ATTO(t)dt \qquad (32)$$

$$\frac{1}{\varphi_i} \int_{t=1}^{\tau} p_i^{Occ}(x,y,t) \cdot ATTO(t)dt = \lambda_i \qquad (33)$$

Where,

φ_i: the normalizing constant

τ: look-ahead-time

φ_i made the risk field satisfy the volume under the $f_i(x,y)$ equal

to λ_i for the object i, as shown in **Equation 34**.

$$\lambda_i = \frac{1}{\varphi_i} \iint \sum_{t=0}^{\tau/\Delta t} p_i^{Occ}(x, y, t) \cdot ATTO(t)\, dxdy \tag{34}$$

Where,

λ_i: risk field intensity parameter

The λ_i differentiates the strength of the risk field depending on the type of object *i*. Note that the crash risk derived **Equation 34** captures overall crash risk that can be extended to other types of conflict pairs.

Assuming that each vehicle generates the same amount of risk field (i.e. they have the same intensity parameter λ_i), the φ_i make the sum of the ATTO to be constant to λ_i regardless of the t_{hl}. One can extend the proposed approach for conflict with other types of road users (e.g., cyclists, pedestrians) simultaneously by adjusting λ_i. For example, one can adjust the level of λ_i for pedestrians 10 times higher than a vehicle, pedestrians generate a 10 times stronger risk field than a vehicle, thereby providing more threat to the drivers

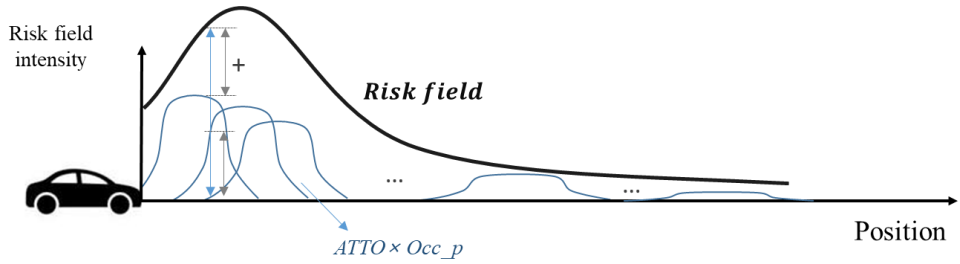

Figure 7. Side view of the risk field

Figure 7 shows a side view of the risk field with its height (i.e., risk field intensity). The height of the risk field can be determined by vehicle mass and types of conflict pairs. In this study, it was assumed that all vehicles emit the same risk with $\lambda = 1.0$.

3.3. RSCF and Approximation

Integrating a value obtained by multiplying the risk field $f_t(x,y)$ by the driver's risk field $g_t(x,y)$ for the inside of the area of the $g_t(x,y)$ can obtain the RSCF. However, computing the exact solution of the double integral is time-consuming and challenging to provide risk assessment in real-time. Therefore, we approximated the double integral using the sampling function of the prediction model. **Equation 35** shows an approximation method using a finite number of summations.

$$RSCF = \iint_{g_t(x,y)} f_t(x,y) g_t(x,y) dxdy \approx \sum_{j=1} \sum_{i=1} f_t(x_i, y_j) g_t(x_i, y_j) \Delta x \Delta \mathrm{y}$$

$$\approx \sum_{j=1} \sum_{i=1} F_t(x_i, y_j) G_t(x_i, x_j) \tag{35}$$

Where,

$F_t(x_i, y_j)$: sample density on the grid of i and j, from $f_t(x,y)$ at time t

$G_t(x_i, x_j)$: sample density on the grid of i and j, from $g_t(x,y)$ at time t

Figure 8 shows the double integral approximation procedure and risk field $F(x_i, y_j)$ and driver's risk field $G(x_i, x_j)$ with grid size.

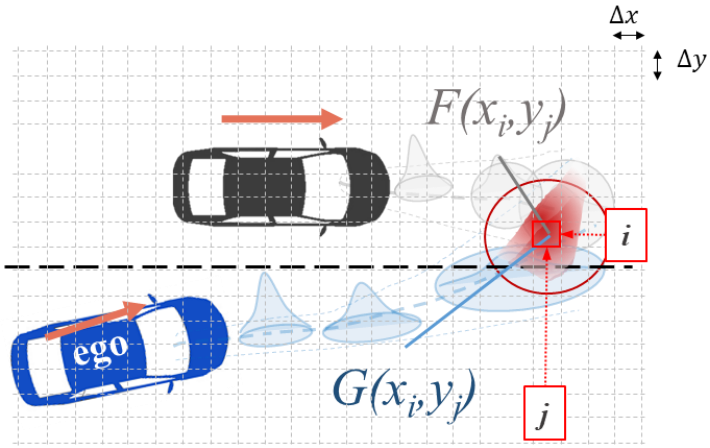

Figure 8. RSCF Approximation procedure

Sampling predictive distribution is a primary factor for convergence speed, which varies depending on the shape of the predictive distribution and the sampling technique. This study adopts the Monte Carlo Markov chain (MCMC) based sampling method to sample points from predictive distribution. Figure 8. Shows 3D representation of risk field and resultant RSCF.

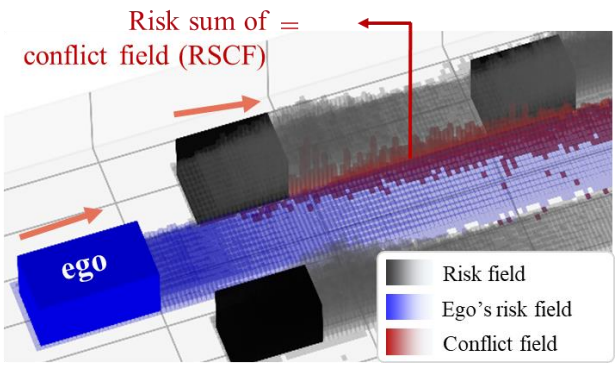

Figure 9. Diagram and implementation of RSCF approximation procedure

3.4. Prediction model

A prediction model is necessary to obtain the future occupancy of the obstacle for constructing the risk field. Recent advances in deep neural network technology have successfully predicted trajectories using a probabilistic approach even in a highly uncertain situation (Bahari et al., 2021; Cui et al., 2019; Deo and TrivediC, 2018; Fu et al., 2021). This study also employs long short-term memory (LSTM) based encoder-decoder networks, effectively capturing vehicle trajectories' spatiotemporal dependencies in the driving scenarios.

The trajectory prediction model performance and risk assessment performance must be closely related (Joo et al., 2021). Recently, the performance of the trajectory prediction model has risen sharply by the availability of high-quality trajectory data and the development of a deep neural network (DNN) framework (Goli et al., 2018; Ma et al., 2019). The DNN generally outperformed conventional trajectory prediction models, including kernel regression, Gaussian process, and auto-regressive integrated moving average (Lefèvre et al., 2014). Among the various DNN framework, the long-short-term-memory (LSTM) and transformer networks have been extensively applied to predict the vehicle's location and speed until more recently (Altche and de La Fortelle, 2018; Lv et al., 2021). For example, the LSTM network

predicted the location and speed of the future 1.0 s in the NGSIM US-101 dataset with an average root mean square of 0.11 m and 0.71 m/s (Altche and de La Fortelle, 2018). A modified LSTM framework predicted the adjacent vehicle's lateral and longitudinal location of six vehicles after 0.5 sec in the NGSIM US-101 dataset with an RMSE of 0.49 m (Fu et al., 2021). Previous studies have shown that the short-term prediction error is even close to the average absolute measurement error in the NGSIM dataset at about 0.5 m in a 1.0 s prediction horizon (Coifman and Li, 2017a).

2.4.1. Inputs and Outputs

Equation 36 shows the input ($\boldsymbol{X}$) and output ($\mathbf{Y}$) for the prediction model used in this study. The T_h and τ indicate observation time for training and prediction horizon, respectively. The prediction model adopted a 0.1-second interval and T_h time-lags of vehicles' location (i.e., x and y coordinates) in the adjacent vehicle for the input. At the prediction time t, the model predicts the vehicles' location at every timestep until the prediction horizon. **Equation 37** shows the input dimension, which is $T_h \times 2 \times N^{veh}$ (T_h timesteps × x, y coordinate × number of vehicles). **Equation 38** shows the output and its dimension, which is $\tau \times 2 \times N^{veh}$ (τ timesteps × x and y coordinates × number of vehicles. As will be covered in Section 3.2.1, we simultaneously

predicted seven vehicles, including the ego vehicle and six adjacent vehicles. Finally, we transformed the locations of the surrounding vehicles to the difference from the ego vehicle to train the network effectively.

$$\boldsymbol{X} = X_{t-T_h}, X_{t-T_h+1}, \dots, X_t, \boldsymbol{Y} = Y_{t+j} \text{ for } j = 1, 2, 3, \dots, \tau \tag{36}$$

$$X_{t_i} = [x_{t-p}^k, y_{t-p}^k] \text{ for } k \in [1, 2, 3, \dots, N^{veh}],\ p \in [0, 1, 2, 3, \dots, T_h] \tag{37}$$

$$Y_{t_{i+j}} = [x_{t+q}^k, y_{t+q}^k] \text{ for } k \in [1, 2, 3, \dots, N^{veh}],\ q \in [1, 2, 3, \dots, \tau] \tag{38}$$

where,

T_h: Observation period (sec)

τ: look-ahead-time (or prediction horizon)

2.4.2. Neural network architecture

Among the variants of LSTMs, the multi-layer Encoder-Decoder LSTM network (EDLN) was empirically found to be effective in extracting the trajectory features in complex scenes and popular for predicting the trajectory (Ettinger et al., 2021; Fu et al., 2021; Saleh et al., 2018). **Figure 10** shows a flow diagram of EDLN composed of four parts: the encoder, decoder, and mixture density network. The multi-layer

LSTM, stacks of LSTMs with the same structure and weights, constitute the encoder and the decoder layer. The historical trajectory data is primarily transformed into a bridge vector by the encoder LSTM. The bridge vector stores the behavioral feature of vehicles in the reference as the input dimension is reduced through the encoder LSTM. The EDLN outputs a vector of vehicles' x and y coordinates in the reference frame through the encoded feature of the bridge vector.

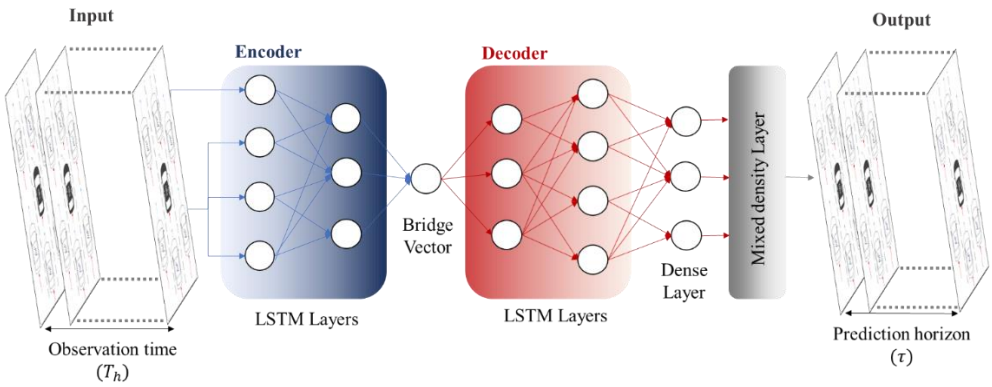

Figure 10. Flow diagram for the EDLN model

After a series of grid searches to select the number of layers and neurons, we adopted 512 neurons and two layers of LSTM and 6 Gaussian mixtures in a mixed density layer to predict the distribution of the x and y coordinates of vehicles. In addition, we fine-tuned the learning rate of the Adam optimizer (Kingma and Ba, 2015) with an initial learning rate of 0.001. We diminished the learning rate by half when there was no improvement in the validation loss for five epochs. To prevent

overfitting, we stopped the training when there was no improvement in the validation loss for ten epochs and then saved the best-trained model. The proposed EDLN method was implemented in the Keras python deep learning library.

2.4.3. Mixture density layer

A prediction model capable of handling the uncertainty in the driving maneuver is a primary interest in recent studies (Bahari et al., 2021; Choi et al., 2021; Deo and Trivedi, 2018). The main reason is that it can simulate scenarios through predictive distribution. It also reflects the multimodality of future maneuvers of a vehicle and the degree of uncertainty (Cui et al., 2019). To this end, we designed a fully connected layer and assigned it to the mixture density layer to predict the distribution of x and y coordinates rather than exact values. We suppose that the x and y coordinates are correlated, and each follows the gaussian mixture distribution, which was often adopted in the literature (Bahari et al., 2021; Fu et al., 2021). Equation 13 shows the predictive distribution of x and y coordinates at time t given the previous trajectories, calculated by the Gaussian mixture distribution. Equation 14 shows the Gaussian distribution used in the Gaussian mixture distribution. **Equation 39-41** shows a normalization process for the Gaussian distribution.

$$\mathrm{P}(x_t, y_t|X) = \sum_{n=1}^{N} w_{t-1}^{n}\, N(x_t, y_t|\boldsymbol{\mu}_{\boldsymbol{t-1}}^{\boldsymbol{n}}, \boldsymbol{\sigma}_{\boldsymbol{t-1}}^{\boldsymbol{n}}, \rho_{t-1}^{n}) \tag{39}$$

$$N\left(x\,, y\,\middle|\boldsymbol{\mu}\,, \boldsymbol{\sigma}\,, \rho\,\right) = \frac{1}{2\pi\sigma_x\sigma_y\sqrt{1-\rho^2}} \exp\left(-\frac{Z}{2(1-\rho^2)}\right) \tag{40}$$

$$Z = \frac{(x-\mu_x)^2}{\sigma_x^2} + \frac{\left(y-\mu_y\right)^2}{\sigma_y^2} - \frac{2\rho(x-\mu_x)(y-\mu_y)}{\sigma_x\sigma_y} \tag{41}$$

Where,

$\boldsymbol{\mu}$, $\boldsymbol{\sigma}$: mean and standard deviation of x and y

w^n: the weight of mixture n

ρ: the correlation coefficient of the x and y.

Equation 42 shows the Gaussian mixture weight $w_{t_i}^n$ estimated via the logit function.

$$w_{t_i}^n = \frac{\exp\left(\hat{w}_{t_i}^n\right)}{\sum_{n'=1}^{N} \exp\left(\hat{w}_{t_i}^{n'}\right)} \tag{42}$$

We adopt the loss function based on the negative log-likelihood loss to train the deep learning network. **Equation 43** shows the loss function (L) for the K vehicles and the N number of the Gaussian mixture.

$$L = \sum_{j=1}^{K} \sum_{t=1}^{T_f} \left[-\log\left(\sum_{n=1}^{N} w_t^{(k),n} N\left(\boldsymbol{X}_{t+1}^{(k)}\middle|\boldsymbol{\mu}_t^{(k),n}, \boldsymbol{\sigma}_t^{(k),n}, \rho_t^{(k),n}\right)\right)\right] \tag{43}$$

.

Chapter 4. Data

4.1. Data Acquisition and Preprocessing

Raw NGISM data has irregular noise and unusual trajectories, including occurrences of abrupt jumps (G. Li et al., 2021b). We filtered out the unrealistic location and acceleration data based on speed measurement data, as it is generally more accurate than location and acceleration measurements (Coifman and Li, 2017; T. Li et al., 2021). To filter out the acceleration measurement data, we applied a threshold of (−5 m/s2 to +4 m/s 2) to the instantaneous acceleration values derived from the speed data and following the procedure and thresholds of the previous study (T. Li et al., 2021). The acceleration value derived from speed was utilized rather than a direct acceleration measurement to detect unrealistic samples. We removed those anomaly points' location, speed, and acceleration measurements and replaced them using linear interpolation with adjacent values.

We filtered out unrealistic location measurement data with speed data. First, we applied a threshold of (±5 m/s), which also followed the threshold of the previous study (T. Li et al., 2021), to find abnormal location data. If the difference between the derived and the measured speed was outside the range, the points were removed and interpolated using linear interpolation. Next, we applied a 0.5 s moving average window to the speed, location, and acceleration data to filter random

noise, considering its robust performance (T. Li et al., 2021). **Figure 11** depicts the results of the above preprocessing for denoising speed and acceleration measurements.

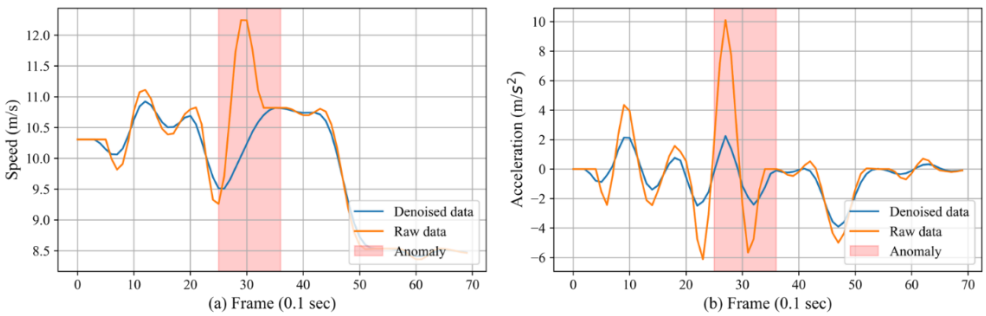

Figure 11. An example of the denoising result of the (a) speed and (b) acceleration measurements

4.2. Test scenario choice

This study employs a top view of the ego vehicle to apply the proposed method. **Figure 12** shows the top view fixed on the blue ego vehicle. The following vehicle (fol) and the preceding vehicle (pre) are labeled based on the y coordinate, and the superscript means the lane. The red line represents the historical trajectory, and the blue line is the trajectory predicted by the model. Assignment in Figure 7 can convert coordinates from the global coordinate system to match the viewpoint of the onboard sensors, including the camera, LiDAR, and radar vehicle (Fu et al., 2021).

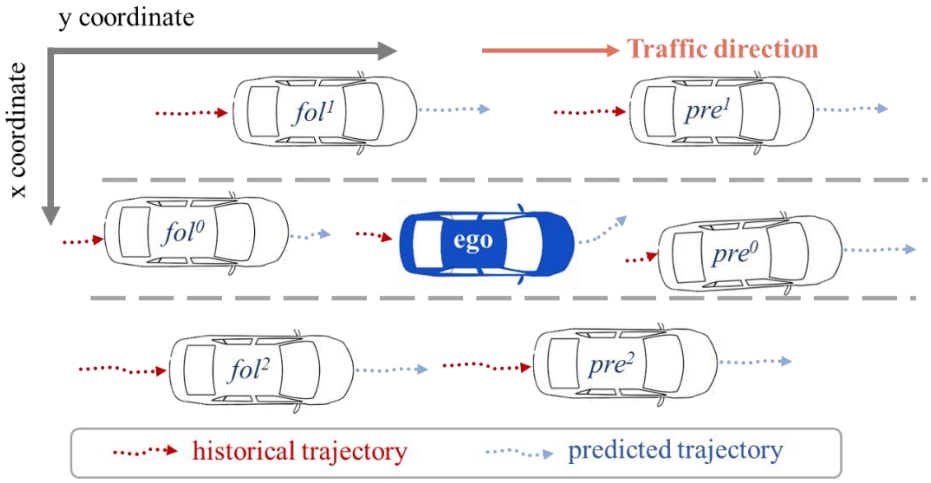

Figure 12. Schematic diagram of the test test scenario assginment.

First, we randomly sampled a vehicle as an ego vehicle. We matched the ego vehicle with other vehicles to form a reference frame. For a case study, this study used 107,034 driving scenarios, which observed 7.0 sec of the reference frame in units of 0.1 sec to avoid a redundant sample. The case studies used 20.8 hours of trajectory data and split the dataset as 80:20 for training and test set.

The safety-related decision-making of AV will arise when it interacts with other human vehicles. Therefore, this study only included highly interactive situations. The TTC, a popular conventional conflict measure on the highway, captures interactions during the observation (Arun et al., 2021b). **Equation 44** represents the TTC of the ego vehicle calculated using the location and speed of the preceding vehicle.

$$TTC_{ego}(t) = \begin{cases} \frac{S_{ego}^{pre^0}(t)}{V_{ego}(t) - V_{pre^0}(t)}, V_{ego}(t) > V_{pre^0}(t) \\ \infty, V_{ego}(t) \leq V_{pre^0}(t) \end{cases} \quad (44)$$

Where,

$S_{ego}^{pre^0}$: the spacing between the ego and the preceding vehicle

V_{ego}, V_{pre^0}: the velocities in the traffic direction of the ego and the preceding vehicle.

In the implementation, the inverse of TTC (1/TTC), a simple but powerful technique to handle the infinity TTC value as the speed difference gets closer to zero, was utilized (Hu et al., 2018; Wang et al., 2021b). We used the average of inverse TTC for 1.0 s before the prediction point (t_0) of the subject vehicle to measure the interaction. Specifically, suppose the mean of the subject vehicle's 1/TTC during previous 1.0 s is less than 10.0 s. In that case, the interaction between the subject and the preceding vehicle is assumed to occur and included in the sample, as shown in **Equation 45**.

$$Interaction = \begin{cases} 1, \mathrm{N}/\sum_{t_0-1.0\,\mathrm{s}}^{t_0}\left(\frac{1}{TTC_{ego}(t)}\right) < 10.0\ s \\ 0, \mathrm{N}/\sum_{t_0-1.0\,\mathrm{s}}^{t_0}\left(\frac{1}{TTC_{ego}(t)}\right) \geq 10.0\ s \end{cases} \quad (45)$$

Figure 13 shows three driving scenarios (i.e., car-following, yielding, and lane-changing) for validating the applicability of the generalized risk assessment of the proposed method. While the car following scenario mainly has a longitudinal direction of conflict, yielding and lane-changing scenarios have an additional lateral direction of conflict. We consider the maneuver as a yielding scenario if the lane number of the preceding vehicle changed and as a lane change scenario if the lane number of the ego vehicle changed.

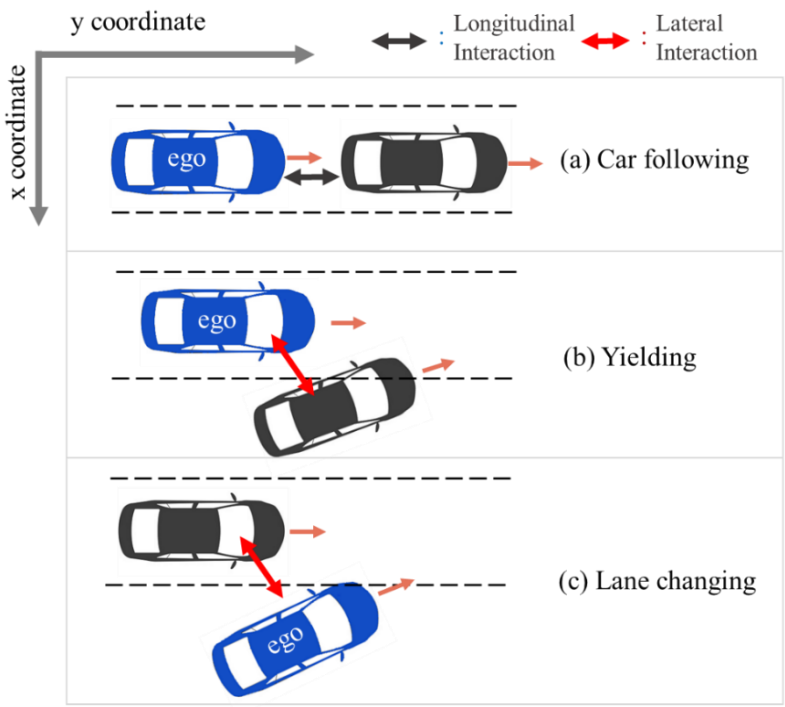

Figure 13. The test scenarios for (a) car-following, (b) yielding, (c) lane-changing

Table 1 summarises the assumption of the parameters in this study. The observation period (T_h) to feed the EDLN network was set as 1.0 s to capture the driver's car-following and lane-change intention. We confirm that more observations for training did not significantly improve the prediction model's performance. Also, the prediction horizon (τ) was set as 6.0 s as any further prediction horizon had little effect on the proposed risk assessment method. In addition, we used 1.0 of risk field intensity (λ) regardless of the vehicle type. We set 0.2 m for a safety margin (δ_{sm}), 2.0 m for standstill distance (δ_{sd}), and 0.5 s for the half-life of the risk field (t_{hl}) to design the shape of the risk field. For the RSCF approximation, we used the approximation grid size of 10 cm × 10 cm, similar to the typical location measurement error in the trajectory dataset (Punzo et al., 2011). Lastly, we utilized 2,000 samples for the approximation, considering computation capacity for the real time application.

Table 1. The Prediction model and risk field parameter list.

Model	Notation	Parameter description	Value
Prediction model	T_h	Observation period	1.0 sec
	τ	Prediction horizon	6.0 sec
Risk field	λ	Risk field intensity	1.0 [-]
	δ_{sm}	Safety margin	0.2 [m]
	δ_{sd}	Standstill distance	2.0 [m]
	thl	Risk field's half-life	0.5 [sec]
	m	Vehicle mass per unit area	100 [kg/m$^{2]}$
RSCF Approximation	$\Delta x \times \Delta y$	Approximation grid size	10×10 [cm^2]
	N_{sim}	Number of MCMC simulation samples	2,000

Chapter 5. Results

5.1. Overview of test scenarios

5.1.1. RSCF visualization

Figure 9 depicts the risk field, driver's risk field, and conflict field generated by the predictive distribution of vehicles in the reference frame for test scenarios. The conflict field (i.e., the red area in **Figure 14**) had a high value where the DRF and the cost field overlap, which intuitively shows that the conflict field occurs at the point where the conflict may occur. In addition, unlike the previous measure that predicts a single point for a conflict point, the conflict field exhibit a distribution of risk depending on the x, y coordinate. These features enabled it to capture various conflicts (e.g., longitudinal, lateral, sideswipe conflict) in a unified way. For example, **Figure 14 (b)** portrays a sideswipe conflict with the preceding vehicle, which cannot be observed in the risk assessment method assuming the vehicle as a point. **Figure 14 (c)** shows the transition from car-following to lane change. It reveals field-based approach has the advantage of taking into account both the lateral and the longitudinal conflicts between all adjacent vehicles in a unified manner.

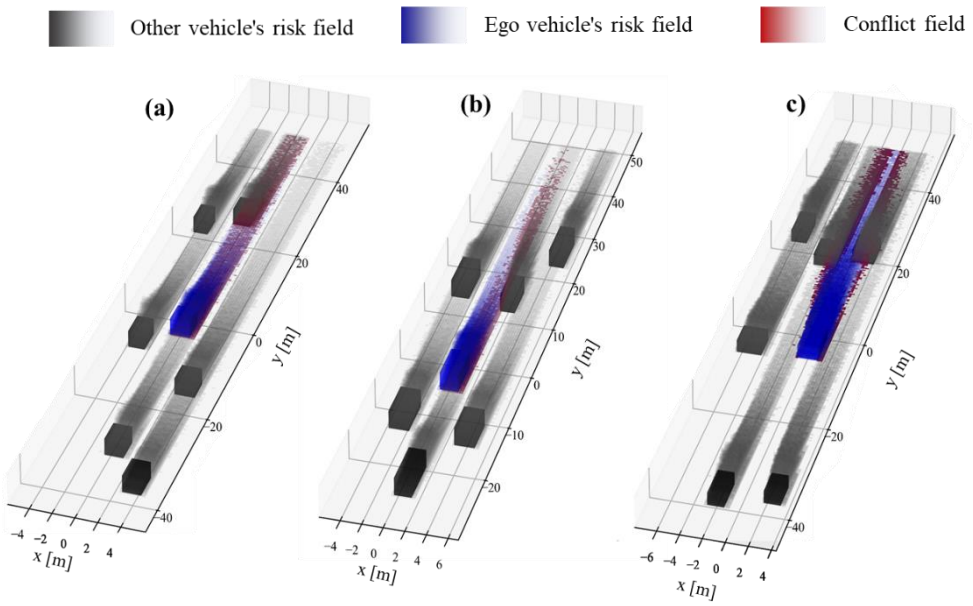

Figure 14. Risk fields for (a) car-following, (b) yielding, and (c) lane-changing scenarios

Note that the RSCF continuously captures overall risk of the current driving scenario every 0.1 sec. It can provide risk profile for crash analysis. Additionally, it represents areas where vehicles should avoid. The vehicle may be driven in a direction that does not overlap with the conflict field or by decelerating to reduce the strength of the RSCF shown in the conflict field.

5.1.2. Convergence test of the RSCF approximation

For the proposed method to be available for the risk assessment of AV, it must satisfy the computational time for real time application (e.g., 0.1 sec). Driving risk assessment is a memory-consuming and computationally intensive routine that occurs parallel to other CAV operations. It includes obstacle tracking, data fusion, module control, and V2X communication.

In this case study, a sample (i.e., MCMC draws) contains 7 vehicles' 6.0 sec of prediction by 0.1-sec interval. We confirmed that the MCMC sampling method obtains RSCF results in about 0.1 seconds (i.e., the temporal resolution of the NGSIM data) for about 2,000 samples. In this experiment, we use the AMD Ryzen 5 3600x and GeForce RTX 2070s. Computation power and its resultant error will be depending on various conditions, but its main factor is the number of samples. Therefore, we used 2,000 samples to construct a risk field and calculate the RSCF regardless of the scenarios.

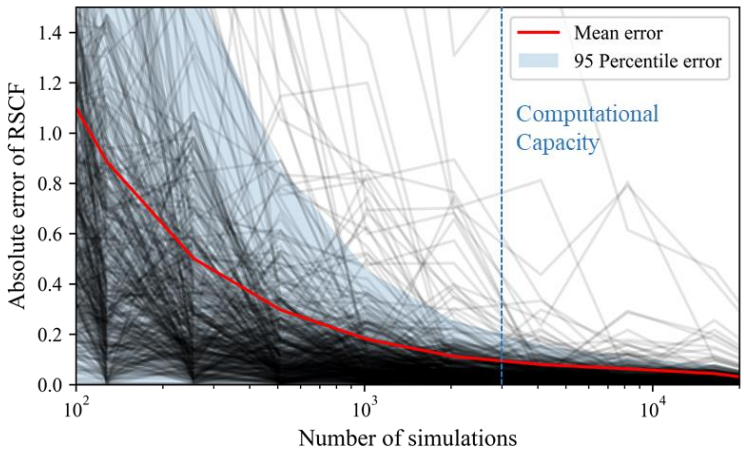

Figure 15. Numerical approximation error according to the number of simulations

As shown in **Figure 15**, 2,000 simulation points resulted in a mean error of less than 0.020, and its 95 percentile was 0.031. The in-depth study of this error was not covered in this study, but should be dealt with in future research. Considering the mean of RSCF is about 0.4, which will be shown in the chapter 4.2, its error will not significantly affect the reliability of approximation. Since proposed method continuously assessed RSCF in 0.1 sec, errorneous will be adjusted shortly. Also, The RSCF value was not a volatile indicator like TTC, and drivers desired a certain level of RSCF. The number of samples produced within the required computation time would increase through optimization or increasing computing power.

5.2. Comparison with SSMs

5.2.1. Risk profile comparison

The risk profile represents the continuous risk estimation trajectory of the current driving circumstance. The risk profile is essential in AV's motion planning algorithms, as it is the criteria for adjusting AV's current motion. Both the proposed method and the conflict indicators can assess the risk of the driving circumstance. Therefore, this section demonstrates the proposed method's strength by comparing the exemplary scenario's risk profile. Figure 14 shows the 4-second risk profile of the scenarios transitioning to the dangerous situation by lane change.

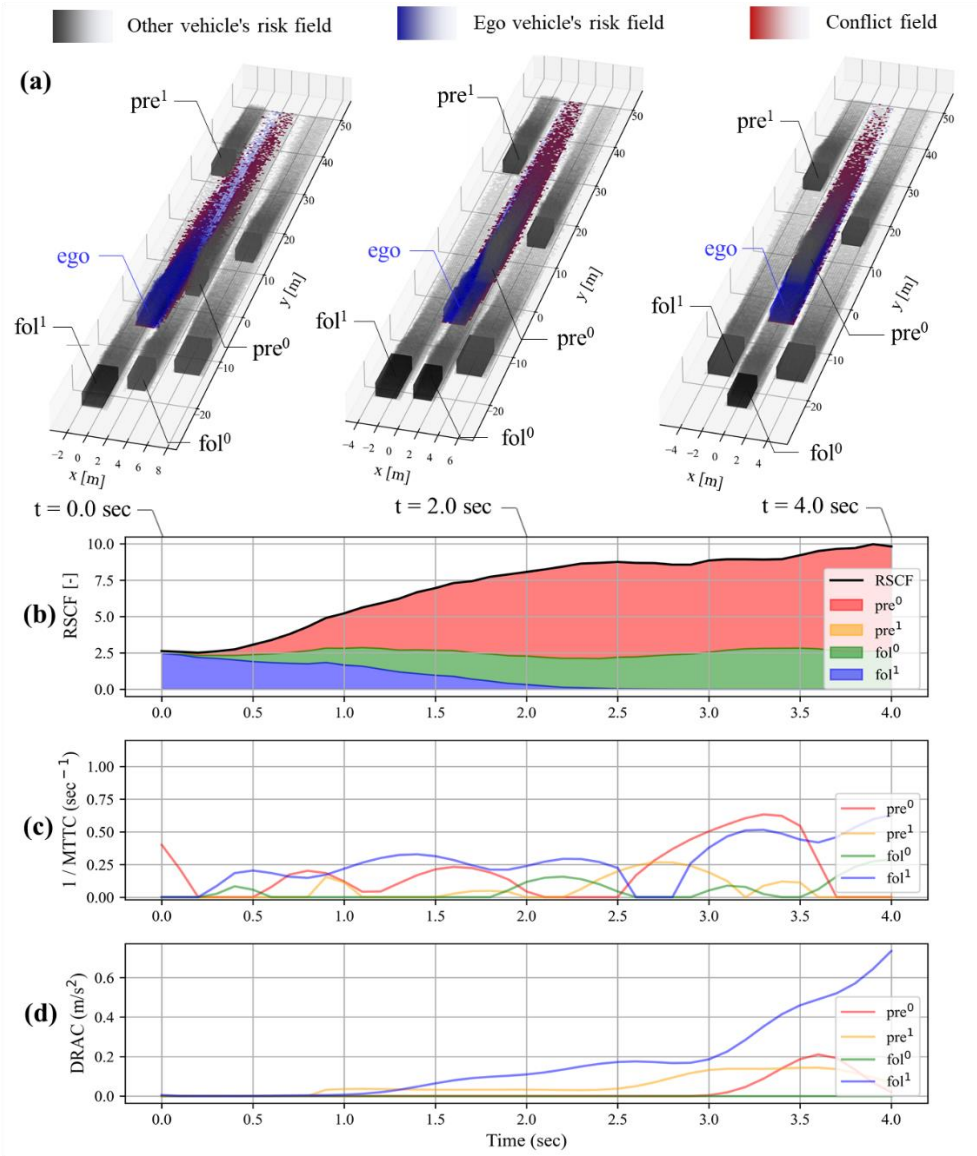

Figure 16. A risk profile of the proposed method, MTTC, and DRAC

Figure 16 primarily represents the risk of lane-changing and pile-up crashes, and there are transitions between the lane-changing and the car-following scenario. In addition, four vehicles simultaneously interact with the ego vehicle during this transition. A sudden interaction, abrupt deceleration, or a crash between the ego and the preceding vehicle can result in another

crash. **Figure 16 (a)** shows risk fields and corresponding conflict of ego vehicle during 4 seconds, and **Figure 16 (b)** shows the resultant RSCF profile of the ego vehicle. The RSCF results from the conflict field continuously estimated the driver's holistic perceived risk. The RSCF reflects the ego vehicle's lateral position as the RSCF has a lower value before the lane change since its previous lane's preceding vehicle (i.e., pre1) is further away. Most conflicts occurred with the following vehicles (i.e., fol1). Then, the RSCF increases as the ego vehicle change lane, caused mainly by the pre0 and fol0 vehicle.

Figures 16 (c) and (d) show conventional conflict indicators (i.e., 1/MTTC and DRAC). Note that we used the inverse of the MTTC to make higher values represent dangerous situations. **Figure 16 (d)** shows that the target lane is not dangerous, as DRAC and MTTC denotes that the presented situation is not critical considering their typical thresholds (Arun et al., 2021b). Note that MTTC and DRAC assess the ego vehicle's risk regardless of the lateral position of the ego vehicle. They are calculated in the same way as if the paths of the vehicle overlap entirely, even if the paths of the vehicle overlap only slightly. This approach overestimates the risk because it is more likely to be avoided if the vehicle's paths overlap only slightly. In addition, the MTTC and DRAC cannot represent a holistic risk when multiple vehicles simultaneously interact since they are essentially derived from an equation for the relationship between two vehicles.

The conflict indicator needs an additional model for the driving risk

of multiple conflicts. For example, the LCRI deploys stopping sight distance of 4 lane change participants to assess the risk of lane-changing (Park et al., 2018). The presented example indicates that erroneous risk assessment results can be obtained if there is a transition between scenarios or if multiple vehicles interact with conventional conflict indicators.

5.2.2. Scenarios comparison

Figure 17 shows the average RSCF of the reference frame according to the scenario. The strength of the proposed methodology is that the RSCF can provide the risk of multiple interactions. In addition, we can decompose the RSCF by individual risks with other vehicles. For example, in the car-following scenario, conflicts with preceding vehicles (i.e., pre^0) and rear vehicles (i.e., fol^0) are dominant. In contrast, most conflicts occur with rear vehicles in yielding scenarios. In the lane-change scenario, there are significantly high-risk estimates in the other (i.e., pre^1, fol^1, pre^2, fol^2). Figure 11 depicts that conflicts usually occur more with the following vehicle than the preceding vehicle, indicating that ego vehicles are relatively insensitive to conflicts with the following vehicle.

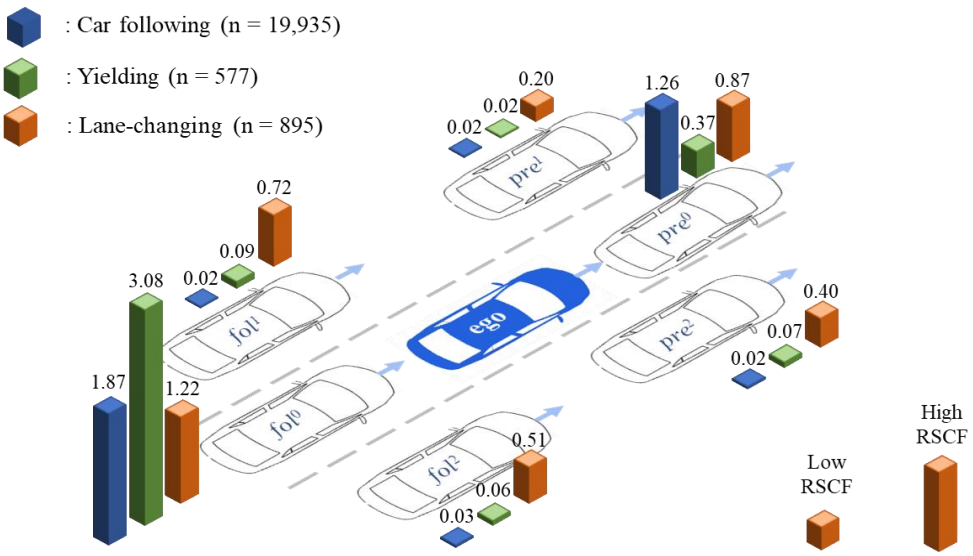

Figure 17. Average RSCF of the adjacent vehicle.

The conflict field continuously provides a probably risky place that drivers may evade and allows AV to carry out safety-adaptive strategies. For example, the conflict field can provide an adaptive sampling strategy for resource-constrained AV sensors. The adaptive sampling strategy devotes extensive computational resources to sensors likely to have informative samples (Nguyen et al., 2016). From the standpoint of vehicle safety, the most informative sample is a dangerous vehicle's maneuver. The quantified risk for each vehicle provides a criterion for increasing the sampling rate or devoting additional processing resources to high-risk vehicle monitoring. It is possible to reduce measurement errors and critical incident identification delays with the adaptive sampling strategy. For instance, preceding and following vehicles occupy most of the risk in the car-following scenario presented in Table 2. AV can allocate resources from sensors that detect other

vehicles to sensors that monitor preceding and following vehicles.

5.2.3. Joint distribution with SSM

The RSCF and traffic conflict indicators correlate since individual traffic conflict indicators partially show a complete safety picture (Arun et al., 2023). The proposed measure captures the holistic driving risk of the ego vehicle during the traffic conflict indicator capturing only one pair at once. Therefore, only the interactions that occur in the current vehicle of the ego vehicle can be compared since the traffic conflict indicator can only be defined if there is a conflict point. **Figure 18** shows the joint distribution of RSCF and the MTTC and DRAC between the preceding vehicle in the current lane (i.e., pre0). Note that we use the inverse of MTTC to make higher values represent higher risk.

Figure 18 shows that the TTC, MTTC, and DRAC are not significantly correlated with RSCF. The main reason for the insignificance is that the RSCF considers the speed and the future position of the vehicles, not the deviation from the speed in its definition, as TTC, MTTC and DRAC do. Also, if there are no differences between acceleration and speed, the MTTC equals 0 independent of the current speed and space between vehicles. In contrast, PET has a distinct positive correlation to the RSCF. The Spearman rank-order correlation coefficient for the RSCF and the PET was 0.837 (p-value < 0.001) in typical car-following scenarios. Therefore, the proposed measure is more relevant to PET rather than other traffic conflict indicators.

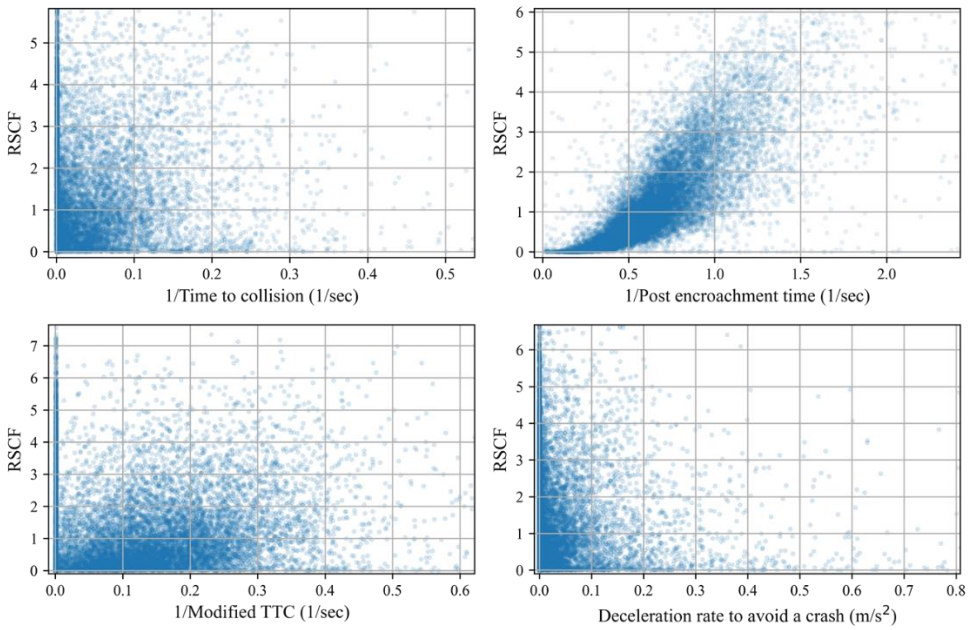

Figure 18. Joint distribution of RSCF and traffic conflict indicators.

One of the major challenges AV faces nowadays is driving in urban environments, where AVs conflict with vehicles and other vulnerable road users, such as passengers, bicyclists, and motorcycles. Conflict indicators were also valuable for setting criteria for pedestrian crash prevention (Rasouli and Tsotsos, 2020). However, there are limitations to quantifying the perceived dangers of pedestrians and passengers in AV. Since pedestrians are free to change directions and have higher uncertainty in their behavior, it may not be appropriate to use conflict indicators that assume constant speed and direction. In particular, a conflict indicator value that forces pedestrians to feel dangerous will differ from that of the driver. For example, the driver feels dangerous about 3 seconds of TTC, while pedestrians may feel dangerous

even at higher TTC. The proposed method evaluates the risk based on its stochastic future position and therefore has the scalability to conflict with other objects in that risk field intensity λ_i weighted the risk differently depending on its property.

5.3. Risk homeostasis

5.3.1. Risk profile

The risk homeostasis theory assumes drivers take evasive actions when the risk they perceive crosses a specific risk level (Ba et al., 2016; Dixit et al., 2019). Therefore, they assumed that drivers maintain a certain level of risk, like body temperature (Wilde', 1982). This study observed that most drivers maintained a certain level of RSCF and thus employed risk homeostasis theory to interpret RSCF value. In other words, drivers prefer a specific volume of the conflict field. Figure 12 shows some examples of the RSCF profiles. It shows that the ego vehicle's driver maintains his RSCF at the desired level and then adjusts the maneuver when the RSCF deviates from its desired level. We defined the desired level of RSCF as the desired RSCF (DRSCF). The mode of the RSCF value during the observation period estimates this study's DRSCF.

The driver's DRSCF is generally stationary during the observation, independent of the location (i.e., lane number, on-off ramp) and adjacent vehicle type (e.g., general vehicle, truck). If the level of subjective risk

perceived exceeds or falls below the driver's desired level, the driver takes steps to eliminate this disparity.

Figure 19 shows several risk homeostasis patterns of RSCF that fluctuate around the DRSCF. **Figure 19 (a)** shows the most prevailing situation in which the value of RSCF is maintained around the DRSCF value. **Figures 19 (b)** and **(c)** show patterns that deviate from the previous DRSCF values due to misperceptions in drivers' perceived risks or changes in DRSCF values. **Figure 19 (d)** shows delayed feedback and overreaction for them (Wilde', 1982). Although these patterns are not clearly distinguished, drivers generally drive along with their DRSCF. One possible explanation for the phenomenon is that the DRSCF indicates the driver's aggressiveness. Depending on the driver's DRSCF value and current RSCF value, drivers can feel dangerous or comfortable.

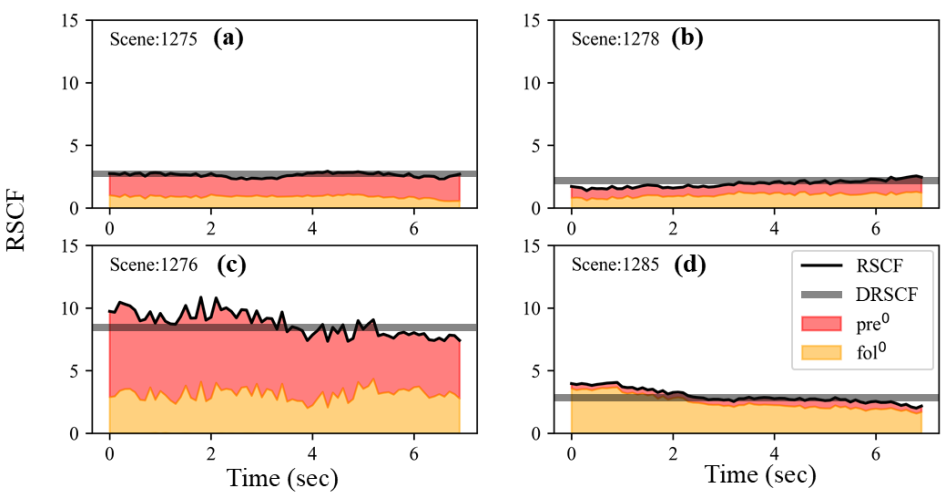

Figure 19. RSCF profiles and the desired RSCF of exemplary scenarios.

5.3.2. Desired and acceptable RSCF

This chapter proposes two methods for standardization of RSCF. The first is to use the desired RSCF, which drivers prefer to maintain, and the second is to use an acceptable RSCF. In the observations in the previous chapter, drivers preferred maintaining a specific RSCF value (i.e., desired RSCF). Likewise, the RSCF value that drivers may bear may also indicate the driver's perceived risk. The RSCF values of the proposed methodology are only relatively comparable and require standardization. The most intuitive standardization method is the proportion of drivers who prefer or can withstand the RSCF.

Figure 20. shows the cumulative distribution function of the desired RSCF and minimum and maximum RSCF during observation. In the risk homeostasis theory, drivers may find it dangerous and adjust their maneuvers if RSCF exceeds the driver's desired RSCF. For example, about 95% of the drivers will feel dangerous when the RSCF exceeds 0.75 and adjust their maneuvers (e.g., slow down or lane change). That will also apply to the customers on AVs.

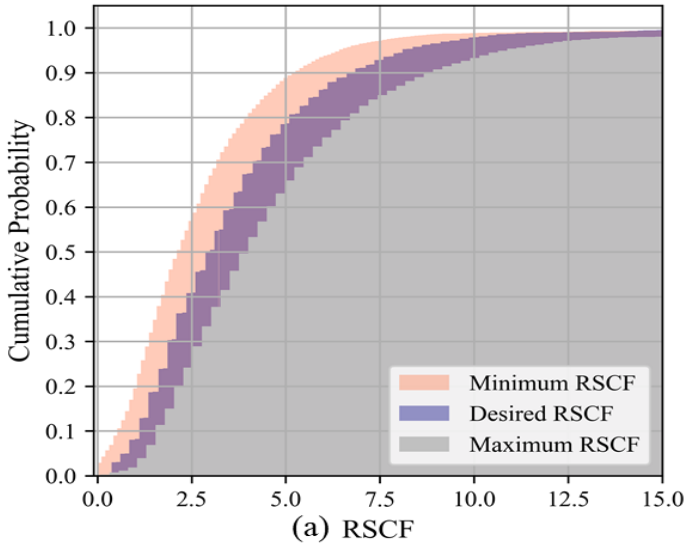

Figure 20. The cumulative distribution function of the RSCF.

Unlike Desired RSCF, maximum RSCF refers to a risk that the driver can afford. The driver will only move below the maximum RSCF value, and if a driver is reached near this value, the driver will not drive above this value. The maximum RSCF is also related to the insurance premium for the AV, as an AV with a higher maximum RSCF will drive aggressively and have a high rate of crashes.

Figure 21 shows an maximum RSCF value according to the scenario. The most conservative operation was performed in the car-following and yielding situations because the maximum RSCF was low. On the other hand, in the Lane changing situation, the maximum RSCF of drivers was relatively high. It indicates that drivers risk more than driving in the same lane in a lane change situation. Therefore, the lane-changing scenario is the most uncomfortable maneuver for drivers. The proposed methodology is for AVs,

but the passenger eventually boards the vehicle. Therefore, setting an appropriate risk limit according to empirical risk acceptance level is essential.

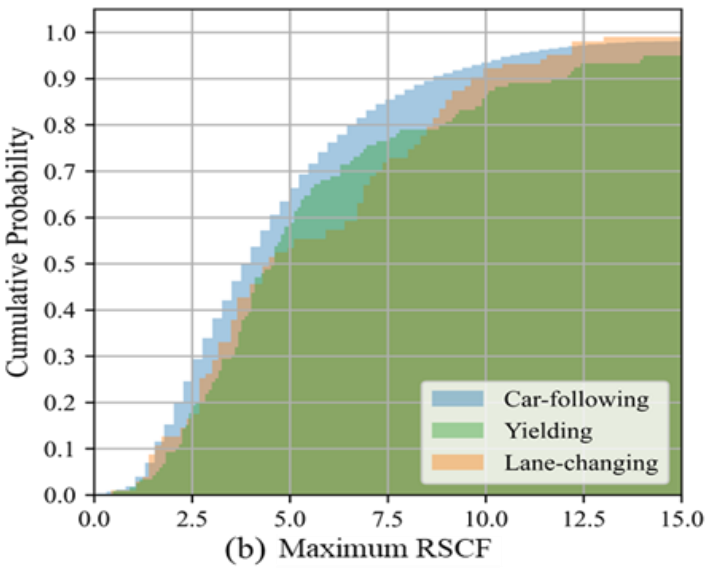

Figure 21. CDF of acceptable RSCF by traffic scenarios

The AVs will have any value for the RSCF like a human driver. If the RSCF value of AV is high and volatile, it probably often exceeds the maximum RSCF for the passengers. AV passengers will not use the AV again if it drives beyond their affordable risk level. Therefore, the level of RSCF an AV should have is critical for passengers to adopt AV. Some consumers will want fast AVs, even if they are dangerous, and others will want slow but safe AVs. One possible option is to allow the driver to select the level of risk (i.e., Desired RSCF) within an allowed range. The DRSCF will also be related to the insurance premium for the AV, as an AV with a higher DRSCF will drive aggressively and have a high rate of crashes.

The association between the RSCF and the actual crash needs further study. The most reasonable way is to assess the prediction capability of the crash (Arun et al., 2023; Zheng and Sayed, 2019). Previous studies adopted extreme value modeling to determine the relationship between the number of crashes and conflict indicators (Arun et al., 2023; Zheng et al., 2019). In the same way, extreme value modeling can be used to define a conflict threshold of the RSCF. However, in the case of AV, it is not easy to collect crash data because crashes do not frequently occur like ordinary drivers. It is challenging to verify the association if sufficient crashes are not collected due to the spatiotemporal instability in accident analysis, as denoted by previous studies (Lord and Mannering, 2010; Mannering, 2018). A possible alternative to validate the proposed method is to relate the driver's subjective perceived risk using a driving simulator (Kolekar et al., 2021, 2020).

5.3. Sensitivity Analysis

5.3.1. Risk field parameters

We designed the risk field based on several assumptions about the parameters (See Table 1), and the most dominant parameter was the half-life parameter (t_{hl}). t_{hl} represents a half-life of the weights for future predictions. Note that the t_{hl} determine the weight of the future risk. The risk field parameter λ and t_{hl} in the conflict field formulation allow for additional extensions for application by considering the heterogeneities regarding the road users and the study site's geography.

Figure 22 shows the effect of t_{hl} by half and twice the assumed value (i.e., t_{hl} = 0.5 sec) in a typical car following scenario. The higher t_{hl} gives higher weight to future occupancy, assuming a conservative driver. On the other hand, low t_{hl} made the current trajectory more critical, which corresponds to the myopic and aggressive driver. High t_{hl} values (≥1.0 sec) require a longer prediction horizon, but this study does not recommend it because most situations will be perceived as dangerous.

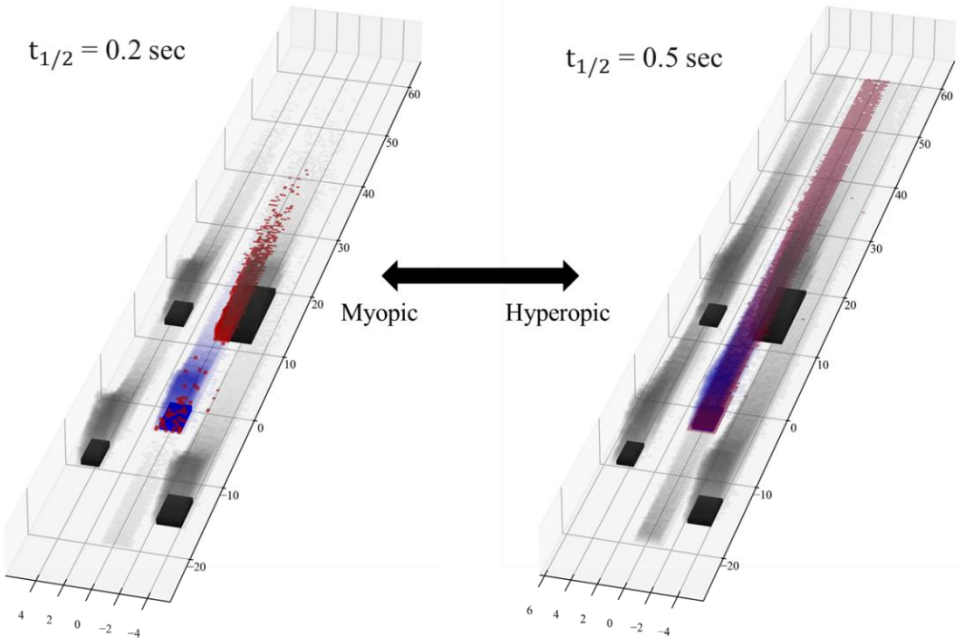

Figure 22. Effect of the half-life of risk field ($t_{1/2}$) parameter

Theoretically, the best way to find a parameter that describes conflict is by using the maximum likelihood method to predict the perceived risk in the study site. Perceived risk can be obtained by electroencephalogram, which captures brain waves. However, measuring the degree of risk, a person feels when putting them in a dangerous situation is impossible. Instead, this study find $\boldsymbol{t_{1/2}}$, which is highly associated with PET. A high correlation with PET is probably not an optimal value. However, if a variable is estimated through a small number of crashes, the variance of the parameter becomes very large (Arun et al., 2023). Assuming that PET represents a part of the conflict, finding $t_{1/2}$ with a high correlation coefficient with PET allows us to find the range of realistic $t_{1/2}$. **Figure 23** shows the Spearman rank order

correlation between RSCF and the traffic conflict indicators depending on the $t_{1/2}$. The higher correlation between the conflict indicator may represent a higher relevance to the actual crashes since each conflict indicator captures a partial crash image. In the tested scenario, the MTTC and 1/TTC are not significantly relevant to the RSCF (i.e., R2 < 0.1) regardless of the $t_{1/2}$. PET and DRAC have similar values, and both are the most relevant at the same value at $t_{1/2}$ = 0.5 sec. Therefore, we recommend 0.5 sec as an appropriate value for $t_{1/2}$.

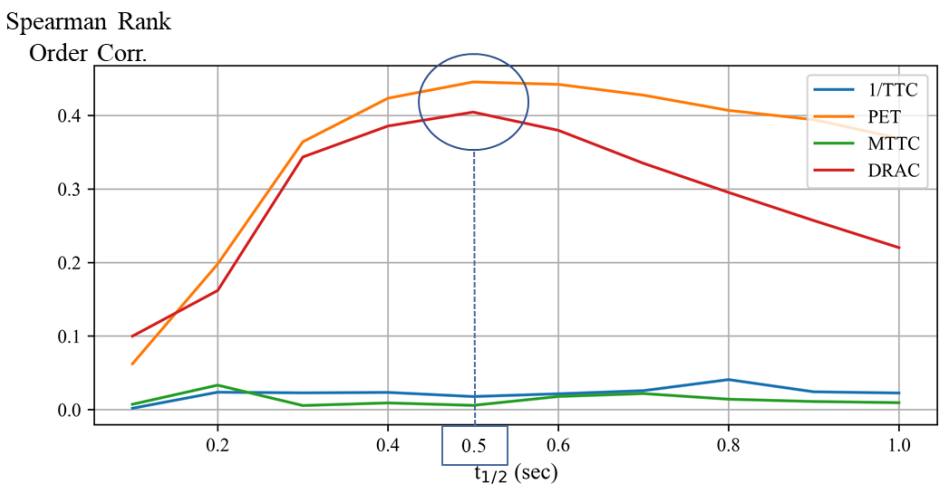

Figure 23 Spearman R with TTC and PET by $t_{1/2}$

Although not covered in this study, selecting a threshold representing conflict is essential in predicting crashes. The previous study used estimation performance for the past crash's occurrence and threshold (Arun et al., 2023; Essa and Sayed, 2019). Such kind of approach is called the peak over

threshold (POT) technique (Zheng and Sayed, 2019). The POT technique uses observations exceeding a predefined threshold as extremes and provides a class of models to enable extrapolation from frequent to infrequent events.

5.3.2. Prediction performance

Another factor contributing risk field is the prediction performance. The performance of the prediction model decreased as the prediction horizon increased. It was estimated that the mean absolute error (MAE) and mean sigma $E(\sigma)$ of predictive distribution in the direction of progress (i.e., the y coordinate) were approximately 15 times greater than those in the lateral direction (i.e., the x coordinate), as shown in **Figure 24**. The MAE and mean sigma $E(\sigma)$ were calculated using E**quations 46-48**.

$$\mu^{pred} = \frac{1}{n_{sim}} \sum_{j}^{n_{sim}} y_j^{samples} \tag{46}$$

$$MAE = \frac{1}{n} \sum_{i=1}^{n} \left| y_i^{true} - \mu_i^{pred} \right| \tag{47}$$

$$E(\sigma) = \frac{1}{n} \sum_{i=1}^{n} \left| y_i^{samples} - \mu_i^{pred} \right| \tag{48}$$

Where,

n_{sim}: Number of MCMC simulations

$y_j^{samples}$: Sample from predicted trajectory distribution

y_i^{true}: True trajectory points

μ_i^{pred}: Mean predicted value

This study predicts the positions and timesteps of multiple vehicles simultaneously, so performance might not be at the state-of-the-art level of the typical single-vehicle prediction models. In addition, we analyzed the situation where the ego vehicle interacted with the surrounding vehicle, and the resulting uncertainty was significant. Therefore, the prediction model's performance was, at best moderate because that model deals with situations that are more difficult to predict because we excluded the normal driving situation.

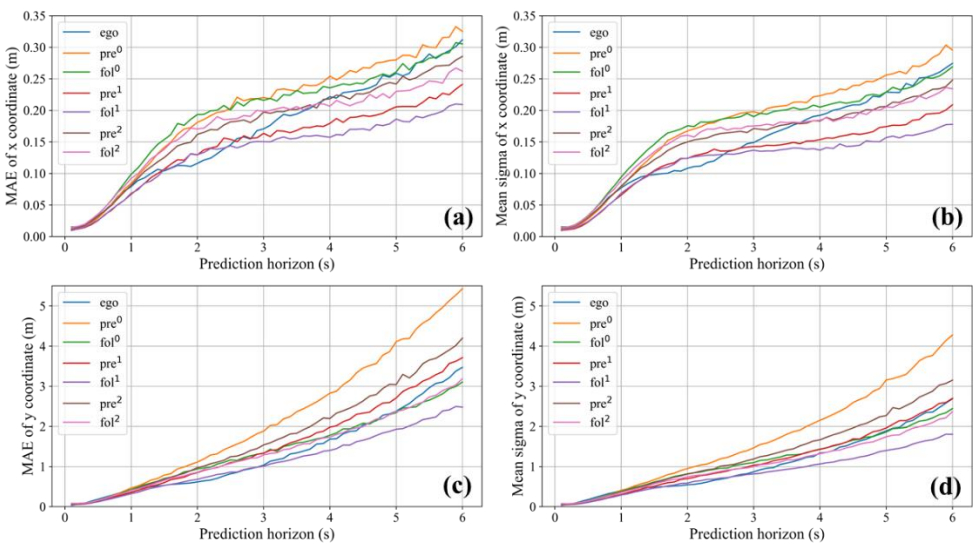

Figure 24. Mean absolute error (a, c) and sigma (b, d) of x, y coordinates in predictive distribution according to the vehicles in the reference frame

Nevertheless, this study investigated the impact of a more accurate predictive distribution model. First, we verified the proposed method using the actual trajectory with a synthetic predictive model. We used bias (b) and

variance (v) parameters to make artificial prediction models that performed better than the presented EDLN. The bias (b) weighted the actual data to the sample mean from the EDLN model, and the variance (v) of the prediction model was multiplied by the residual when creating an artificial model, as shown in **Equation 49**. Therefore, if bias and variance are both 1.0, they correspond to the EDLN model, and if bias and variance are both 0, then they are the same as the actual trajectory.

$$\hat{y}_{syn}^{sample} = b \times \mu^{sample} + (1 - b) \times y^{true} + v(y^{sample} - \mu^{pred}) \quad (49)$$

Bias and variance affect the shape of the risk field and the resultant RSCF. **Figure 25** shows the effect of bias and variance on the risk field design and the RSCF in the exemplary scenario with a synthetic predictive model. In this scenario, the predictive model has a more significant bias and a variance in RSCF compared to the average scenario. The more significant variance in the ego vehicle caused the DRF to distribute sparsely, as shown in **Figures 25 (a)** and **(b)**. Therefore, when bias increases, the mean absolute error (MAE) and the false alarm increase, while a blurry risk estimate is inevitable when the variance increases. In other words, low bias and variance in the prediction model make the risk assessment model distinguish between hazardous and non-critical situations (Joo et al., 2021).

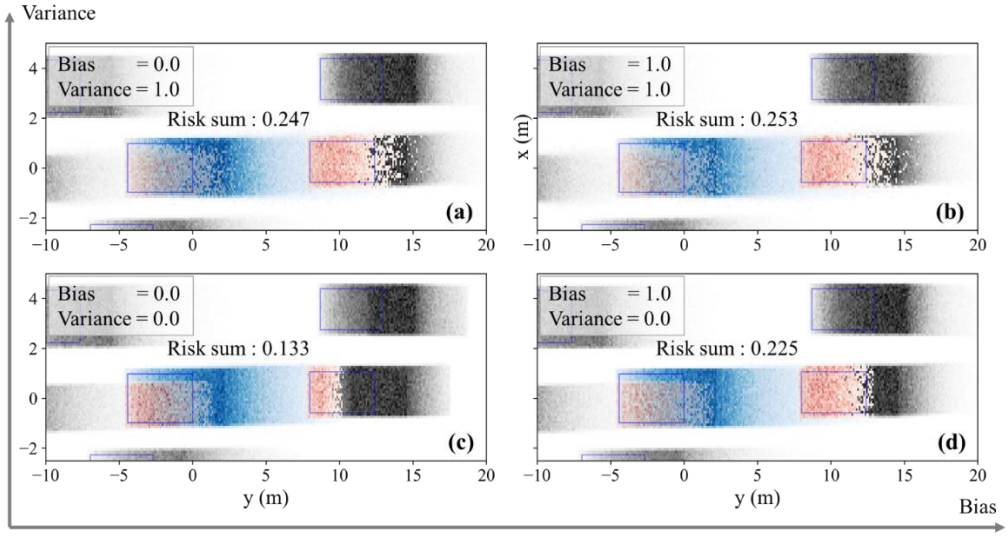

Figure 25. Effect of bias and variance of the prediction model on the risk field and RSCF

Chapter 6. Conclusions and Future Research

6.1. Conclusion

This study proposed a method for assessing the crash risk when using autonomous vehicles (AVs). The assessment is based on the concept of field theory, which is a way of modeling the interactions between the adjacent vehicle of AV. In this approach, artificial fields are used to calculate the crash risk, taking into account the interactions between the different fields with the conflict field. The conflict field provides a quantified risk estimate (i.e., RSCF) that can be used as criteria for the AV passenger's comfort. In addition, we introduce a mathematical framework for approximating proposed measures for real-time application. We demonstrate our work in risky highway scenarios and compare the conventional conflict-based measures.

The advantage of this method is that it represents the appearance of the dangerous area to the passenger of the AV, independent of the conflict type and the traffic scenario. Additionally, the use of field theory allows for a more flexible and adaptable approach, as various types of road users or transitions between scenarios can be easily incorporated into the assessment.

As a result, this study makes several contributions to the risk assessments of AVs. First, this study provides a generalized risk assessment method for seamlessly evaluating an AV's driving risk without scenario identification (e.g., car-following and lane-changing). Second, the conflict

field intuitively visualizes its potential conflict points with intensity in a 3-dimensional risk field, imitating the driver's subjective risk perception procedure. Lastly, the conflict field jointly estimates conflict with all adjacent vehicles and imposes higher risk estimates on multiple conflicts.

It should be noted that this is an academic method and might not be implemented in real-world scenarios yet. Further research and development would be required for its application in practical autonomous driving systems. We relied on assumptions and parameters to operationalize the framework, and these parameters can be optimized using crash data or the perceived risk observed by the electroencephalography (EEG) or driving simulator. In addition, this study only proposed a risk field formulation and verified it in the homogeneous highway. Several other traffic scenarios, such as interactions with bicycles and pedestrians, may be further validated. Further investigation of interactions between static objects such as road boundaries and traffic signals would also provide implications for driving risks in mixed traffic conditions.

Using data from connected and automated vehicles (CAV) to create the risk field model is an attractive future research opportunity since CAVs can provide an accurate driver and vehicle information absent from this study (e.g., blinker). The visualized risk field can be utilized in the human-machine interface (HMI) in AV to overcome consumers' psychological barriers and fears.

6.2. Future research

In light of the aforementioned, there are opportunities for further development. For instance, the scope of the current work was limited to the development of a risk field formulation and subsequent conflict-force models for highway interactions. However, various other traffic scenarios, such as pedestrian-vehicle interactions, may require alternative characteristics for defining the conflict. Due to an insufficient sample size for relevant crash data, the study was unable to quantify the effects of altering variables such as speeding, even for rear-end collisions. Consequently, these parameters should be explored to improve the precision and accuracy of crash-risk modeling. Future studies should also investigate the vehicle features pertinent to other evasive maneuvers, such as swerving and acceleration. In addition, the traffic flow parameter might further increase the accuracy of road user movement modeling utilizing the safety field approach. Using data from connected and autonomous vehicles (CAV) to create the risk field model is an attractive future research possibility since CAVs can provide the missing accurate driver and vehicle information from the existing specification. By merging CAV data with data from IoT-enabled roadside cameras and LIDAR units, a fully described risk field model could revolutionize the analysis of real-time road safety for both connected cars and unequipped road users such as pedestrians and cyclists.

Reference

Altche, F., de La Fortelle, A., 2018. An LSTM network for highway trajectory prediction. IEEE Conference on Intelligent Transportation Systems, Proceedings, ITSC 2018-March, 353–359. https://doi.org/10.1109/ITSC.2017.8317913

Arun, A., Haque, Md.M., Washington, S., Mannering, F., 2023. A physics-informed road user safety field theory for traffic safety assessments applying artificial intelligence-based video analytics. Anal Methods Accid Res 37, 100252. https://doi.org/10.1016/j.amar.2022.100252

Arun, A., Haque, Md.M., Washington, S., Sayed, T., Mannering, F., 2022. How many are enough?: Investigating the effectiveness of multiple conflict indicators for crash frequency-by-severity estimation by automated traffic conflict analysis. Transp Res Part C Emerg Technol 138, 103653. https://doi.org/10.1016/j.trc.2022.103653

Arun, A., Haque, M.M., Bhaskar, A., Washington, S., Sayed, T., 2021a. A systematic mapping review of surrogate safety assessment using traffic conflict techniques. Accid Anal Prev 153, 106016. https://doi.org/10.1016/j.aap.2021.106016

Arun, A., Haque, M.M., Washington, S., Sayed, T., Mannering, F., 2021b. A systematic review of traffic conflict-based safety measures with a focus on application context. Anal Methods Accid Res 32, 100185. https://doi.org/10.1016/j.amar.2021.100185

Bahari, M., Nejjar, I., Alahi, A., 2021. Injecting knowledge in data-driven vehicle trajectory predictors. Transp Res Part C Emerg Technol 128, 103010. https://doi.org/10.1016/j.trc.2021.103010

Ba, Y., Zhang, W., Chan, A.H.S., Zhang, T., Cheng, A.S.K., 2016. How drivers fail to avoid crashes: A risk-homeostasis/perception-response

(RH/PR) framework evidenced by visual perception, electrodermal activity and behavioral responses. Transp Res Part F Traffic Psychol Behav 43, 24–35. https://doi.org/10.1016/j.trf.2016.09.025

Chen, Q., Huang, H., Li, Y., Lee, J., Long, K., Gu, R., Zhai, X., 2021. Modeling accident risks in different lane-changing behavioral patterns. Anal Methods Accid Res 30. https://doi.org/10.1016/j.amar.2021.100159

Choi, S., Kweon, N., Yang, C., Kim, D., Shon, H., Choi, J., Huh, K., 2021. DSA-GAN: Driving Style Attention Generative Adversarial Network for Vehicle Trajectory Prediction. IEEE Conference on Intelligent Transportation Systems, Proceedings, ITSC 2021-Septe, 1515–1520. https://doi.org/10.1109/ITSC48978.2021.9564674

Coifman, B., Li, L., 2017a. A critical evaluation of the Next Generation Simulation (NGSIM) vehicle trajectory dataset. Transportation Research Part B: Methodological 105, 362–377. https://doi.org/10.1016/j.trb.2017.09.018

Coifman, B., Li, L., 2017b. A critical evaluation of the Next Generation Simulation (NGSIM) vehicle trajectory dataset. Transportation Research Part B: Methodological 105, 362–377. https://doi.org/10.1016/j.trb.2017.09.018

Cui, H., Radosavljevic, V., Chou, F.C., Lin, T.H., Nguyen, T., Huang, T.K., Schneider, J., Djuric, N., 2019. Multimodal trajectory predictions for autonomous driving using deep convolutional networks. Proc IEEE Int Conf Robot Autom 2019-May, 2090–2096. https://doi.org/10.1109/ICRA.2019.8793868

Deo, N., Trivedi, M.M., 2018. Multi-Modal Trajectory Prediction of Surrounding Vehicles with Maneuver based LSTMs. IEEE Intelligent Vehicles Symposium, Proceedings 2018-June, 1179–1184. https://doi.org/10.1109/IVS.2018.8500493

Dixit, V., Xiong, Z., Jian, S., Saxena, N., 2019. Risk of automated

driving: Implications on safety acceptability and productivity. Accid Anal Prev 125, 257–266. https://doi.org/10.1016/j.aap.2019.02.005

Essa, M., Sayed, T., 2019. Full Bayesian conflict-based models for real time safety evaluation of signalized intersections. Accid Anal Prev 129, 367–381. https://doi.org/10.1016/j.aap.2018.09.017

Essa, M., Sayed, T., 2015. Transferability of calibrated microsimulation model parameters for safety assessment using simulated conflicts. Accid Anal Prev 84, 41–53. https://doi.org/10.1016/j.aap.2015.08.005

Ettinger, S., Cheng, S., Caine, B., Liu, C., Zhao, H., Pradhan, S., Chai, Y., Sapp, B., Qi, C., Zhou, Y., Yang, Z., Chouard, A., Sun, P., Ngiam, J., Vasudevan, V., McCauley, A., Shlens, J., Anguelov, D., 2021. Large Scale Interactive Motion Forecasting for Autonomous Driving : The Waymo Open Motion Dataset.

Fu, C., Sayed, T., 2022. Bayesian dynamic extreme value modeling for conflict-based real-time safety analysis. Anal Methods Accid Res 34, 100204. https://doi.org/10.1016/j.amar.2021.100204

Fu, M., Zhang, T., Song, W., Yang, Y., Wang, M., 2021. Trajectory Prediction-Based Local Spatio-Temporal Navigation Map for Autonomous Driving in Dynamic Highway Environments. IEEE Transactions on Intelligent Transportation Systems 1–12. https://doi.org/10.1109/TITS.2021.3057110

Goli, S.A., Far, B.H., Fapojuwo, A.O., 2018. Vehicle Trajectory Prediction with Gaussian Process Regression in Connected Vehicle Environment. IEEE Intelligent Vehicles Symposium, Proceedings 2018-June, 550–555. https://doi.org/10.1109/IVS.2018.8500614

Hu, Y., Zhan, W., Tomizuka, M., 2018. Probabilistic Prediction of Vehicle Semantic Intention and Motion. IEEE Intelligent Vehicles Symposium, Proceedings 2018-June, 307–313. https://doi.org/10.1109/IVS.2018.8500419

Joo, Y.J., Park, H.C., Kho, S.Y., Kim, D.K., 2021. Reliability-based assessment of potential risk for lane-changing maneuvers. Transp Res Rec 2675, 161–173. https://doi.org/10.1177/03611981211010800

Katrakazas, C., Quddus, M., Chen, W.H., Deka, L., 2015. Real-time motion planning methods for autonomous on-road driving: State-of-the-art and future research directions. Transp Res Part C Emerg Technol 60, 416–442. https://doi.org/10.1016/j.trc.2015.09.011

Kim, J., Kum, D., 2018. Collision Risk Assessment Algorithm via Lane-Based Probabilistic Motion Prediction of Surrounding Vehicles. IEEE Transactions on Intelligent Transportation Systems 19, 2965–2976. https://doi.org/10.1109/TITS.2017.2768318

Kingma, D.P., Ba, J.L., 2015. Adam: A method for stochastic optimization. 3rd International Conference on Learning Representations, ICLR 2015 - Conference Track Proceedings 1–15.

Kolekar, S., de Winter, J., Abbink, D., 2020. Human-like driving behaviour emerges from a risk-based driver model. Nat Commun 11. https://doi.org/10.1038/s41467-020-18353-4

Laureshyn, A., de Ceunynck, T., Karlsson, C., Svensson, Å., Daniels, S., 2017. In search of the severity dimension of traffic events: Extended Delta-V as a traffic conflict indicator. Accid Anal Prev 98, 46–56. https://doi.org/10.1016/j.aap.2016.09.026

Lee, K., Kum, D., 2019. Collision avoidance/mitigation system: Motion planning of autonomous vehicle via predictive occupancy map. IEEE Access 7, 52846–52857. https://doi.org/10.1109/ACCESS.2019.2912067

Lee, Y.C., Momen, A., LaFreniere, J., 2021. Attributions of social interactions: Driving among self-driving vs. conventional vehicles. Technol Soc 66. https://doi.org/10.1016/j.techsoc.2021.101631

Lefèvre, S., Sun, C., Bajcsy, R., Laugier, C., 2014. Comparison of

parametric and non-parametric approaches for vehicle speed prediction. Proceedings of the American Control Conference 3494–3499. https://doi.org/10.1109/ACC.2014.6858871

Li, G., Yang, Y., Zhang, T., Qu, X., Cao, D., Cheng, B., Li, K., 2021a. Risk assessment based collision avoidance decision-making for autonomous vehicles in multi-scenarios. Transp Res Part C Emerg Technol 122, 102820. https://doi.org/10.1016/j.trc.2020.102820

Li, G., Yang, Y., Zhang, T., Qu, X., Cao, D., Cheng, B., Li, K., 2021b. Risk assessment based collision avoidance decision-making for autonomous vehicles in multi-scenarios. Transp Res Part C Emerg Technol 122, 102820. https://doi.org/10.1016/j.trc.2020.102820

Li, T., Chen, D., Zhou, H., Laval, J., Xie, Y., 2021. Car-following behavior characteristics of adaptive cruise control vehicles based on empirical experiments. Transportation Research Part B: Methodological 147, 67–91. https://doi.org/10.1016/j.trb.2021.03.003

Lv, Z., Huang, X., Cao, W., 2021. An improved GAN with transformers for pedestrian trajectory prediction models. International Journal of Intelligent Systems 1–20. https://doi.org/10.1002/int.22724

Machado-León, J.L., De Oña, J., De Oña, R., Eboli, L., Mazzulla, G., 2016. Socio-economic and driving experience factors affecting drivers' perceptions of traffic crash risk. Transp Res Part F Traffic Psychol Behav 37, 41–51. https://doi.org/10.1016/j.trf.2015.11.010

Mannering, F.L., Bhat, C.R., 2014. Analytic methods in accident research: Methodological frontier and future directions. Anal Methods Accid Res 1, 1–22. https://doi.org/10.1016/j.amar.2013.09.001

Ma, Y., Qin, X., Grembek, O., Chen, Z., 2018. Developing a safety heatmap of uncontrolled intersections using both conflict probability

and severity. Accid Anal Prev 113, 303–316. https://doi.org/10.1016/j.aap.2018.01.038

Ma, Y., Zhu, X., Zhang, S., Yang, R., Wang, W., Manocha, D., 2019. TrafficPredict: Trajectory prediction for heterogeneous traffic-agents. 33rd AAAI Conference on Artificial Intelligence, AAAI 2019, 31st Innovative Applications of Artificial Intelligence Conference, IAAI 2019 and the 9th AAAI Symposium on Educational Advances in Artificial Intelligence, EAAI 2019 6120–6127. https://doi.org/10.1609/aaai.v33i01.33016120

Mullakkal-Babu, F.A., Wang, M., He, X., van Arem, B., Happee, R., 2020. Probabilistic field approach for motorway driving risk assessment. Transp Res Part C Emerg Technol 118, 102716. https://doi.org/10.1016/j.trc.2020.102716

Nguyen, L. v., Kodagoda, S., Ranasinghe, R., Dissanayake, G., 2016. Information-Driven Adaptive Sampling Strategy for Mobile Robotic Wireless Sensor Network. IEEE Transactions on Control Systems Technology 24, 372–379. https://doi.org/10.1109/TCST.2015.2435657

Park, H., Oh, C., Moon, J., Kim, S., 2018. Development of a lane change risk index using vehicle trajectory data. Accid Anal Prev 110, 1–8. https://doi.org/10.1016/j.aap.2017.10.015

Rahman, M.S., Abdel-Aty, M., Lee, J., Rahman, M.H., 2019. Safety benefits of arterials' crash risk under connected and automated vehicles. Transp Res Part C Emerg Technol 100, 354–371. https://doi.org/10.1016/j.trc.2019.01.029

Saleh, K., Hossny, M., Nahavandi, S., 2018. Intent prediction of vulnerable road users from motion trajectories using stacked LSTM network. IEEE Conference on Intelligent Transportation Systems, Proceedings, ITSC 2018-March, 327–332. https://doi.org/10.1109/ITSC.2017.8317941

Shariff, A., Bonnefon, J.F., Rahwan, I., 2021. How safe is safe enough? Psychological mechanisms underlying extreme safety demands for self-driving cars. Transp Res Part C Emerg Technol 126. https://doi.org/10.1016/j.trc.2021.103069

Shi, X., Wong, Y.D., Li, M.Z.F., Chai, C., 2018. Key risk indicators for accident assessment conditioned on pre-crash vehicle trajectory. Accid Anal Prev 117, 346–356. https://doi.org/10.1016/j.aap.2018.05.007

Taeihagh, A., Lim, H.S.M., 2019. Governing autonomous vehicles: emerging responses for safety, liability, privacy, cybersecurity, and industry risks. Transp Rev 39, 103–128. https://doi.org/10.1080/01441647.2018.1494640

Tan, H., Lu, G., Liu, M., 2021. Risk Field Model of Driving and Its Application in Modeling Car-Following Behavior. IEEE Transactions on Intelligent Transportation Systems 1–16. https://doi.org/10.1109/tits.2021.3105518

Venthuruthiyil, S.P., Chunchu, M., 2022. Anticipated Collision Time (ACT): A two-dimensional surrogate safety indicator for trajectory-based proactive safety assessment. Transp Res Part C Emerg Technol 139, 103655. https://doi.org/10.1016/j.trc.2022.103655

Wang, C., Stamatiadis, N., 2014. Derivation of a New Surrogate Measure of Crash Severity. Transportation Research Record: Journal of the Transportation Research Board 2432, 37–45. https://doi.org/10.3141/2432-05

Wang, C., Sun, Q., Fu, R., Li, Z., Zhang, Q., 2018. Lane change warning threshold based on driver perception characteristics. Accid Anal Prev 117, 164–174. https://doi.org/10.1016/j.aap.2018.04.013

Wang, C., Xie, Y., Huang, H., Liu, P., 2021a. A review of surrogate safety measures and their applications in connected and automated vehicles safety modeling. Accid Anal Prev 157.

https://doi.org/10.1016/j.aap.2021.106157

Wang, C., Xie, Y., Huang, H., Liu, P., 2021b. A review of surrogate safety measures and their applications in connected and automated vehicles safety modeling. Accid Anal Prev 157, 106157. https://doi.org/10.1016/j.aap.2021.106157

Wilde', G.J.S., 1982. The Theory of Risk Homeostasis: Implications for Safety and Health, Risk Analysis.

Zheng, L., Sayed, T., 2019. Comparison of Traffic Conflict Indicators for Crash Estimation using Peak Over Threshold Approach. Transp Res Rec 2673, 493–502. https://doi.org/10.1177/0361198119841556

국문초록

본 연구는 운전자 지원 및 자율주행 시스템에서 차량이 직면하는 주행상황의 위험을 평가하기 위해 고속도로에서 발생할 수 있는 시나리오에서 여러 차량과의 충돌을 시각적으로 포착하는 일반화된 방법을 제공한다. 이를 위해, 본 연구는 장이론 기반의 접근법을 활용한다. 리스크 필드 접근법은 장애물의 예측 위치를 사용하여 장애물이 발산하는 위험감을 나타내는 장을 스칼라 필드(리스크 필드)로 정의한다. 물체들에서 발생되는 리스크 필드의 중첩에 의해 발생하는 상충의 강도을 정량화하기 위해 운전자의 주관적 위험 인식을 포착하는 상충 필드라는 수정된 위험 필드를 제안한다. 제안된 상충 필드는 충돌의 정도를 평가할 수 있는 시각적으로 직관적인 근거를 제공하고 실시간으로 주행상황의 위험을 선제적으로 정량화할 수 있다.

제안된 방법론을 검증하기 위해 고속도로 주행 데이터를 사용하여 세 가지 주행 상황(즉, 차량 추종, 양보 및 차선 변경)에 대한 기존 안전성 평가방법론과 비교했다. 결과적으로 제안된 방법은 단일 위험 상호 작용보다 여러 위험 상호 작용에 더 높은 위

험을 가지는 것으로 평가하며 일반적으로 PET와 일관된 결과를 도출한다. 마지막으로, 민감도 분석을 통해 주요 모수의 가정과 예측 모형에서 발생한 편향과 분산에의 영향을 평가하였다. 본 연구의 주된 학술적인 기여는 인접 차량과의 다양한 유형의 다중 충돌 상황을 동시에 평가하고 잠재적 충돌 위치를 제공하는 것이다. 또한 제안된 운전 위험 평가 방법은 통합되고 일반화된 방식으로 자율주행차 시스템에 효과적이고 안정적인 안전 기준을 제공함으로서 자율주행 산업에 있어서 기여할 수 있을 것으로 기대된다.

주요어: 리스크 필드, 일반화된 위험성 평가, 대리안전지표, 교통 상충, 실시간 안전성 평가

학번: 2018-27038

Acknowledgement

저는 이곳에 이 글을 작성하기 까지 많은 도움을 받았습니다. 저의 20대가 온전히 담긴 졸업논문에 그 감사를 표하는 것은 제 인생에서 진심 어린 감사를 표할 수 있는 몇 안되는 소중한 기회라고 생각합니다. 그러니 그간 받아온 큰 도움에 대한 감사를 이 짧은 글로 담아내는 것을 부디 너그러이 양해를 부탁드립니다. 이 글에서는 그간 대학원에서의 여정을 되돌아보며 감사의 인사를 드리려 합니다.

대학교 2학년 시절부터 지금까지 만날 줄 모르고 같이 밴드하며 즐기던 우리 밴드는 어느덧 모두 박사가 되었습니다. 비록 분야는 다르지만 대학원 선배로서, 인생 선배로서, 그리고 친구로서 지내온 김선명, 배성한, 손용하, 최홍영 박사님에게 감사드립니다. 앞으로도 자주 볼 수 있으면 좋겠습니다.

연구실에 들어와서는 철도 없고 모르는 것도 많았습니다. 그보다 더 큰 문제는 제가 그러한 상황인지 모르는 것이었습니다. 선배들이 말씀주시던 경험이 쌓이면 알게 되는 것들이 분명히 있더라는 말씀을 당시에는 이해하지 못했습니다. 부끄럽지만 대학원 생활을 하다 보니 어느덧 후배들에게 같은 이야기를 하고 있습니다. 돌이켜보니 지도교수님이신 김동규 교수님과 고승영 교수님께서 팀장이나 연구실 실장으로서 증명할 기회를 흔쾌히 허락하신 것 덕분이라고 생각합니다. 졸업논문을 마무리 하는 지금 되돌아보면, 그 기회는 더할나위 없이 좋은 추억이자 배움이었습니다.

다들 그러하겠지만, 누군가의 사수가 된다는 것은 무수한 생각을 하게 했습니다. 제가 그 누군가의 인생에 있어 지대한 영향을 미칠 것이라는 것은 때로는 무거운 짐이 되었기도 했습니다. 부족한 팀장이었던 제게 선배로서의 자세에 대해 고민하게 해주었던, 후배이자 선배였던 정욱, 용우, 재원이형, 그리고 준희와 성연이에게 감사드립니다. 연구실에서의 길다면 긴 5년동안 서로 배려하며 별 탈 없이 지낼 수 있었던 것도 능력있고 자상한 동기들 덕분이었습니다. 그중에서 특히

앞으로 저와 비슷한 길을 걸어갈 세동이, 기택이, 산업계에서 큰 역할을 기대할 승우에게도 꼭 고맙다고 말하고 싶습니다.

졸업에 가까워지면서는 감사하게도 교수님들께 참 많은 도움을 받았던 것 같습니다. 졸업논문 작성과 연구진행에 있어 큰 도움 주셨던 박신형 교수님과 박영진 교수님, 연구실 생활동안 학문적 스승이 되어 주셨던 박호철 교수님과 김의진 교수님, 그리고 졸업심사와 더불어 플로리다에서 생활할 수 있도록 지원해주신 박준영 교수님께도 깊은 감사의 말씀 드립니다. 교수님들께서 주셨던 무조건적인 도움을 절대 잊지 않고, 후배들에게도 베풀 것을 다짐하겠습니다.

제가 멀리 떨어진 고등학교에 진학하겠다고 했었을 때에도, 이곳 학부를 오겠다고 할 때도, 대학원에 진학하겠다고 할 때도, 그리고 미국으로 떠나겠다는 제 결정을 항상 믿고 존중해주시며 물심양면으로 지원해주신 아빠와 엄마, 그리고 할머니와 이모할머니, 고모께서 주신 사랑을 평생 잊지 않겠습니다. 항상 따스한 말로 다정하게 대해주시고 저희를 지원해주시는 장모님과 장인어른께도 감사의 말씀 드립니다. 사랑합니다.

마지막으로, 저를 위해 먼 곳 플로리다에서 고생하고 있는 아내 지희에게 무엇보다 큰 감사를 드립니다. 아무래도 저의 졸업은 지희가 아니었다면 상상할 수 없었던 것 같습니다. 같은 학문의 길을 걷는 지희를 옆에 두지 않았다면, 이 길을 평생 걸어갈 용기가 나지 않았을 것입니다. 철부지같던 저에 대한 지희의 확고한 믿음과 사랑은 앞으로 수십년간 함께 살아갈 용기를 얻는데 부족함이 없었습니다. 지금 간직하고 있는 지희에 대한 이 고마움을 평생 잊지 않고 사랑하며 살아가겠습니다.

2023년 2월 6일